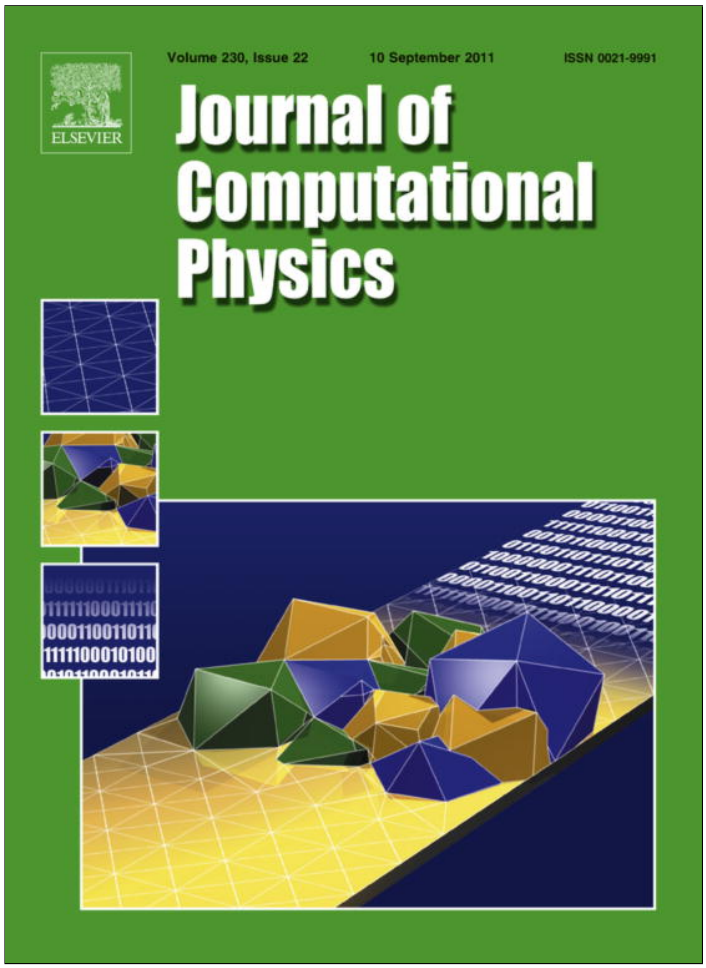

Journal of Computational Physics 230 (2011) 8109–8133

Contents lists available at ScienceDirect

Journal of Computational Physics

journal homepage: www.elsevier.com/locate/jcp

An accurate and efficient method for treating aerodynamic interactions of cloud droplets

B. Rosa [a,b], L.-P. Wang [a,*], M.R. Maxey [c], W.W. Grabowski [d]

[a] Department of Mechanical Engineering, University of Delaware, Newark, DE 19716, USA
[b] Institute of Meteorology and Water Management, ul. Podlesna 61, 01-673 Warsaw, Poland
[c] Division of Applied Mathematics, Brown University, Providence, RI 02912, USA
[d] Mesoscale and Microscale Meteorology Division, National Center for Atmospheric Research, P.O. Box 3000, Boulder, CO 80307-3000, USA

ARTICLE INFO

Article history:
Received 21 March 2011
Received in revised form 12 July 2011
Accepted 16 July 2011
Available online 27 July 2011

Keywords:
Collision efficiency
Aerodynamic interaction
Lubrication force
Stokes flow
Hybrid approach

ABSTRACT

Motivated by a need to improve the representation of short-range interaction forces in hybrid direct numerical simulation of interacting cloud droplets, an efficient method for treating the aerodynamic interaction of two spherical particles settling under gravity is developed. An effort is made to ensure the accuracy of our method for any inter-particle separation by considering three separation ranges. The first is the long-range interaction where a multipole method is applied. After a decomposition into six simple configurations, explicit formulae for drag forces and torques are derived from an approximate Force–Torque–Stresslet (FTS) formulation. The FTS formulation is found to be accurate when the separation distance normalized by the average radius is larger than 5. The second range concerns the short-range interaction where the interaction force could be very large. Leading-order lubrication expansions are employed for this range and are found to be accurate when the normalized separation is less than about 0.01. Finally, for the intermediate range where no simple method is available, a third-order polynomial fitting is proposed to bridge the treatments for long-range and short-range interactions. After optimizing the precise form of polynomial fitting and matching locations, the force representation is found to be highly accurate when compared with the exact solution for Stokes flows. Using this method, collision efficiencies of cloud droplets sedimenting under gravity have been calculated. It is shown that the results of collision efficiency are in excellent agreement with results based on the exact Stokes flow solution. Collision efficiency results are also compared to previous results to further illustrate the accuracy of our calculations. The effects of particle rotation and the attractive van der Waals force on the collision efficiency are also studied. The efficient force representation developed here is more general than the usual lubrication expansion and thus can serve as a better approach to correct unresolved short-range interactions in particle-resolved simulations.

1. Introduction

In recent years an increasing number of studies have been initiated to quantify the effects of air turbulence on the growth of cloud droplets during warm rain initiation, as it is believed that the in-cloud turbulence can enhance the rate of collision–coalescence and as such provides a mechanism to overcome the bottleneck between the diffusional growth and the

* Corresponding author. Tel.: +1 302 831 8160; fax: +1 302 831 3619.
E-mail address: lwang@udel.edu (L.-P. Wang).

0021-9991/$ - see front matter © 2011 Elsevier Inc. All rights reserved.
doi:10.1016/j.jcp.2011.07.012

gravitational collision–coalescence mechanism (see [1,2] and references therein). Cloud droplets of radius less than 10 μm grow efficiently through diffusion of water vapor, and droplets larger than 50 μm in radius grow efficiently through gravitational collisions [3]. Much recent attention has therefore been directed to the enhanced collision–coalescence rate by air turbulence for cloud droplets in the size range from 10 to 50 μm in radius. It has been shown that a moderate enhancement (*i.e.*, by a factor of two to three) of the collision kernel by air turbulence can significantly accelerate the growth of cloud droplets to form drizzle drops [2,4,5].

Air turbulence can enhance the collision–coalescence rate in two general ways. First, for the simplified problem of geometric collision neglecting aerodynamic interaction of cloud droplets, air turbulence can increase the collision rate by three possible mechanisms (see [2,4] and references therein): (1) enhanced relative motion due to differential acceleration and shear effects; (2) enhanced average pair density (*i.e.*, the number of interacting droplet pairs per unit volume) due to local preferential concentration of droplets; and (3) enhancement due to selective alterations of the settling rate by turbulence. Second, air turbulence can alter the collision efficiency of cloud droplets [6], namely, the ratio of the number of droplet pairs that can come into contact under the influence of local aerodynamic interaction, to the number of colliding droplet pairs without considering the local aerodynamic interaction. Air turbulence affects the collision efficiency by (1) enhancing the far-field relative motion of droplets and (2) introducing local flow shear and acceleration which modifies the aerodynamic interaction forces on droplets.

Compared to the geometric collision, collision efficiency is a more difficult problem as the disturbance flows introduce another set of length and time scales in addition to the background air turbulence. While there are quite a few studies in the literature concerning the collision efficiency of cloud droplets without air turbulence, there are very few studies devoted to the collision efficiency in a turbulent flow (e.g., see [6] and references therein). As pointed out in [7], previous studies often predicted different levels of enhancement of collision efficiency. This in part results from different kinematic formulations used to define the collision efficiency in different studies, some of which are not applicable to turbulent collisions. More importantly, there is currently a lack of accurate and consistent representations of aerodynamic interaction of many droplets in a turbulent flow.

As a first step in developing a better computational method for treating aerodynamic interaction of cloud droplets in a turbulent flow, an improved superposition method (ISM) was introduced in [8] to quantify the collision efficiency of cloud droplets in still air. The basic idea is to impose, in some average sense, the no-slip boundary condition on the surface of each droplet to better determine the magnitude and coupling of the Stokes disturbance flows in a many-droplet system. The no-slip boundary condition is specified either at the center of each droplet (the center-point formulation) or by an integral average over the droplet surface (the integral formulation). The advantage of ISM is that the application to many-droplet interactions in a turbulent airflow is rather straightforward leading to a hybrid direct numerical simulation (HDNS) approach [9,10]. The HDNS approach combines direct numerical simulation of the background air turbulence with an analytical representation of the disturbance flow introduced by many droplets. The approach takes advantage of the fact that the disturbance flow due to droplets is localized in space and there is a sufficient length-scale separation between the droplet size and the Kolmogorov scale of the background turbulent flow. This hybrid approach provides, for the first time, a consistent, quantitative tool for studying the combined effects of air turbulence and aerodynamic interactions on the motion and collisional interactions of cloud droplets. The disturbance flow is coupled with the background air turbulence through the approximate implementation of the no-slip boundary conditions on each droplet. Dynamical features in three dimensions and on spatial scales ranging from a few tens of centimeters down to 10 μm are captured. Both the near-field and the far-field droplet–droplet aerodynamic interactions could be incorporated [11].

HDNS provides a framework for a systematic improvement of the approach. In this regard, the HDNS approach is closely related to the multipole expansion method [12], also in general known as the *Stokesian dynamics* approach [13]. In fact, the center-point formulation of ISM is essentially the zero-moment expansion with only monopole terms and without the Faxen correction [14,15], while the integral formulation of ISM is the zero-moment expansion with the Faxen correction since the integral average of disturbance flow velocity over a droplet surface is equivalent to the center-point velocity plus the Faxen term. Here moments mean the force moments in the multipole expansion of Stokes flow solution around rigid particles [12]. Durlofsky et al. [12] presented a multipole formulation known as the Force–Torque–Stresslet (FTS) formulation which includes moments up to the first-order plus Faxen terms. This multipole expansion method considers many-body interaction with Stokes disturbance flows superimposed onto a nonuniform background flow.

The authors of [8,12] recognized that ISM and FTS cannot handle correctly short-range or lubrication forces. The short-range interaction forces, in principle, would require all higher-order moments to be included in the multipole expansion [16]; and the convergence to the exact lubrication forces is usually slow in the multipole expansion approach [17,16]. To accurately treat the lubrication force, Durlofsky et al. [12] made use of the exact force representation of the two-sphere problem (e.g., [17,18]) and at the same time, properly remove the redundant part from the multipole many-body representation. This procedure could be complicated for the many-droplet problem.

As a logical next step to the ISM, in this paper, we develop an efficient approach for two-droplet aerodynamic interaction in still air with accurate force representation for all separation distances. The results will be compared against the exact solutions of Jeffrey and Onishi [17] (Hereafter will be referred to as JO84). Our approach is to divide the problem into three subproblems. First, for long-range interactions, we apply FTS to six independent, simple configurations (see Fig. 1) which then in linear combination can be used to handle any long-range interaction of two unequal-size droplets. Second, the short-range interaction will be treated by a few leading order terms from the explicit lubrication expansion of JO84. Then guided by the

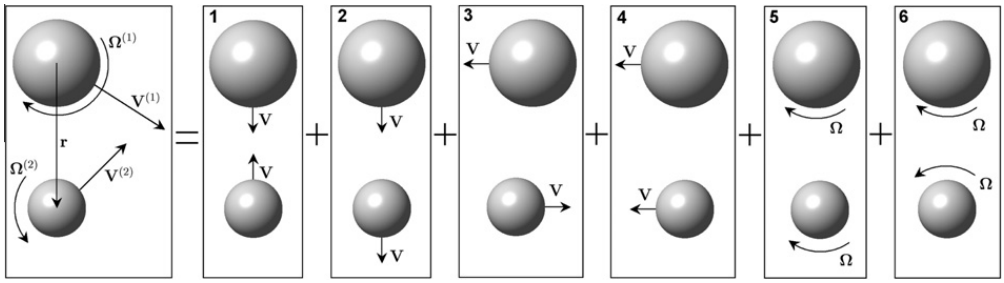

Fig. 1. Treating arbitrary two-body configuration by combining six simple interactions.

JO84 exact solutions, we develop an optimized, empirical matching procedure for the intermediate separation ranges. We then apply this approach to compute collision efficiencies of two sedimenting droplets in still air and compare our results to previous theoretical results in [19,20]. We will also include van der Waals forces in our approach and compare our results with those in [21]. The establishment of such an efficient method is a necessary step towards improving our HDNS approach, particularly in treating short-range many-droplet interactions in a turbulent flow.

One limitation of the proposed approach is the assumption of Stokes disturbance flows, which is known to become inaccurate for droplets larger than 30 μm in radius [22]. On one hand, currently, no known method can treat, in an efficient manner, the problem of many-droplet interactions beyond Stokes disturbance flows. The work of Klett and Davis [22] represents the first study in which the leading-order fluid-inertia (or finite droplet Reynolds number) effect in the disturbance flows is considered for two-droplet interaction by using Oseen flow equations. Several attempts [23–27] were made to handle two-droplet aerodynamic interaction at finite Reynolds numbers using a simple superposition method in which the disturbance flow due to each droplet is computed numerically by solving nonlinear Navier–Stokes equations, without any influence by the disturbance flow due to the other droplet. Unfortunately, such a simple superposition method has been widely criticized as it can result in an unphysical collision efficiency [26], and it is known to be very inaccurate even for Stokes disturbance flows [8]. It is not surprising that no attempt has been made to adapt this simple superposition method to many-droplet interactions.

This paper is organized as follows. In Section 2 we present the detailed formulation of the method and how it is applied to different interaction configurations. Optimization of the matching locations are discussed in Section 3.1, the accuracy of force representation for the resulting model is shown in Section 3.2, and its application to collision efficiency prediction is described in Section 3.3 along with detailed comparison with previously published results. The effects of droplet rotation and van der Waals force are briefly elucidated as well. Finally, Section 4 contains a summary and concluding remarks.

2. Methodology

Consider the relative motion of two aerodynamically interacting cloud droplets of radii a_1 and a_2 ($a_1 \geqslant a_2$). The droplets are suspended in an otherwise stagnant viscous air of viscosity $\mu \approx 1.7 \times 10^{-5}$ kg m^{-1} s^{-1} and density $\rho = 1.0$ kg m^{-3}, and move in response to the action of their own inertia, added mass, Stokes drag, the gravity force, and the buoyancy force. The droplet density is $\rho_p = 1000$ kg m^{-3}. It is assumed that droplets remains spherical since under the typical conditions of atmospheric cloud droplets the capillary pressure is several orders of magnitude larger than the local fluid shear stress induced by the disturbance flow associated with droplet sedimentation. For example, for a droplet of 30 μm in radius, the capillary pressure, $P_c = 2\sigma/a$, is roughly 4800 Pa, while the viscous shear stress may be estimated as $\sim\mu W/a$ and is only about 0.05 Pa. Here σ and W are the surface tension and droplet terminal velocity, respectively. In addition, the dynamic viscosity of water is about 55 times the dynamic viscosity of air, numerical solutions [28] show that the effect of internal flow circulation can be safely neglected and the droplets can be treated as rigid particles, for all droplets of radius less than 150 μm. Note that the Stokes flow solution considering both flow outside and inside a small spherical water droplet settling at a terminal velocity W would predict a maximum velocity of $W/[2(1+\gamma)] \approx 0.0089W$ on the surface of the droplet, where γ is the viscosity ratio ($\sim$55). Therefore, in this paper droplets are treated as rigid particles and the two terms "droplet" and "particle" will be used interchangeably. A rather thorough discussion on the validity of the rigid sphere assumption including droplet internal circulation, distortion from a spherical shape, and shape oscillation for larger drops can be found in [28].

It is further assumed that the radius of the droplets does not exceed 30 μm so that the terminal velocity is of the order of 0.1 m s^{-1} or less and as such the droplet Reynolds number is small [29]. The disturbance flow acting on the droplets due to their relative motion is represented by a Stokes flow solution. The motion of the droplets can be determined numerically by solving the equations of motion in the form

$$m_p^{(\alpha)}\left(1+0.5\frac{\rho}{\rho_p}\right)\frac{dV_i^{(\alpha)}(t)}{dt} = F_i^{(\alpha)} + m_p^{(\alpha)}\left(1-\frac{\rho}{\rho_p}\right)\mathbf{g}, \tag{1}$$

$$I_p^{(\alpha)} \frac{d\Omega_i^{(\alpha)}(t)}{dt} = L_i^{(\alpha)}, \tag{2}$$

$$\frac{dY_i^{(\alpha)}(t)}{dt} = V_i^{(\alpha)}(t); \tag{3}$$

where $m_p^{(\alpha)}$ is mass of the αth droplet, V_i and Ω_i denote the droplet velocity and angular velocity, respectively, F_i is a viscous force and L_i is a torque exerted by the fluid on the droplets, I_p is the moment of inertia, and Y_i is the droplet location. We assume that the background air velocity is zero. Eq. (1) is the Newton's 2nd law, with the buoyancy force and the added mass being separated out from the viscous hydrodynamic force. The added mass and the buoyancy force are negligibly small since they are proportional to ρ/ρ_p.

The equations of motion, Eqs. (1)–(3), were solved with the following initial conditions: the larger droplet was placed at $\mathbf{Y}^{(1)}(t=0) = [0,0,0]$ and the smaller droplet at $\mathbf{Y}^{(2)}(t=0) = [0,\delta,l]$; where the vertical separation distance l was set to $50a_1$; the initial horizontal displacement δ was equal to the average value of the droplet radii $\hat{a} \equiv \frac{1}{2}(a_1 + a_2)$; the z axis was assumed to point downward along the gravity direction. The horizontal separation was adjusted to either 2δ or 0.5δ after the first trial, depending on whether this initial setting would lead to coalescence. Due to symmetry, calculation of collision efficiency in stagnant air can be reduced to a quasi-two-dimensional problem, with droplets moving only in the y–z plane and rotating around the axis parallel to the x direction. The initial velocities were set to $V_3^{(1)}(0) = W^{(1)} + \frac{3}{2}\frac{a_1}{l}W^{(2)}$ and $V_3^{(2)}(0) = W^{(2)} + \frac{3}{2}\frac{a_2}{l}W^{(1)}$, where $W^{(1)}$ is terminal velocity of the larger droplet and $W^{(2)}$ the terminal velocity of the smaller droplet. The above prescription of initial droplet velocities includes the leading-order long-range Stokes-flow interaction and ensures that the results of particle trajectories and collision efficiency are independent of the initial vertical separation distance.

The fundamental problem in treating the interaction between two rigid particles is the efficient calculation of the force $\mathbf{F}^{(\alpha)}$ and torque $\mathbf{L}^{(\alpha)}$ exerted by the fluid on the particles. For the case of Stokes disturbance flow, an exact solution for the two-particle problem is available in the literature. For example, JO84 presented an exact solution based on a bi-spherical expansion method which may require summation of a large number of terms in the expansion. The general multipole expansion method for Stokes flows [30,12] can also be used to treat the interaction of two and more particles. In order to achieve a high computational efficiency, here we propose to combine the second order multipole expansion method of Durlofsky et al. [12] which is quite accurate for large separations, with analytical expansions accurate for short separations based on JO84. A method for constructing an accurate force representation for intermediate separations will be developed here.

The use of different strategies for different separations was previously considered in [21]. Davis calculated drag force using two asymptotic solutions from JO84, assumed to be valid for $s > 4$ and $s < 2.01$, respectively. Here s is defined as the dimensionless distance between centers of the spheres $s = r/\hat{a}$, where r is the distance between the centers of droplets. For the intermediate range, $2.01 < s < 4$, where the number of terms in the series must be relatively large, Davis interpolated the interaction force from pretabulated values.

In our approach the entire problem of 3D motion was first decomposed into six easier subproblems, as shown in Fig. 1. Such a decomposition greatly simplifies force and torque calculations and is justified because the Stokes flow equation is linear. Each of the six subproblems is treated separately. In the first case, the two droplets approach each other from opposite directions with the same velocity. This is the case where the interaction force can increase rapidly in proportion to the inverse of the separation gap distance when the gap distance approaches zero (e.g., see [30]). In the second case droplets move with the same velocity in the same direction along the line of centers. The other two cases describe the motion perpendicular to the line of centers, with the third case for droplets moving in opposite directions and the fourth in the same direction. The last two cases are related to particle rotational motion. Case 5 handles rotational motion of both particles in the same direction with equal angular velocities and finally Case 6 the rotational motion in the opposite directions each with equal angular velocity. In vector form the decomposition as applied to the larger particle can be written as follows:

$$\begin{aligned}\mathbf{V}^{(1)} &= \frac{\mathbf{V}^{(1)} - \mathbf{V}^{(2)}}{2} + \frac{\mathbf{V}^{(1)} + \mathbf{V}^{(2)}}{2} \\ &= \underbrace{\frac{(\mathbf{V}^{(1)} - \mathbf{V}^{(2)})\cdot\mathbf{e}_r}{2}\mathbf{e}_r}_{\text{Case 1}} + \underbrace{\left[\frac{\mathbf{V}^{(1)} - \mathbf{V}^{(2)}}{2} - \frac{(\mathbf{V}^{(1)} - \mathbf{V}^{(2)})\cdot\mathbf{e}_r}{2}\mathbf{e}_r\right]}_{\text{Case 3}} + \underbrace{\frac{(\mathbf{V}^{(1)} + \mathbf{V}^{(2)})\cdot\mathbf{e}_r}{2}\mathbf{e}_r}_{\text{Case 2}} + \underbrace{\left[\frac{\mathbf{V}^{(1)} + \mathbf{V}^{(2)}}{2} - \frac{(\mathbf{V}^{(1)} + \mathbf{V}^{(2)})\cdot\mathbf{e}_r}{2}\mathbf{e}_r\right]}_{\text{Case 4}},\end{aligned} \tag{4}$$

$$\mathbf{\Omega}^{(1)} = \underbrace{\frac{\mathbf{\Omega}^{(1)} + \mathbf{\Omega}^{(2)}}{2}}_{\text{Case 5}} + \underbrace{\frac{\mathbf{\Omega}^{(1)} - \mathbf{\Omega}^{(2)}}{2}}_{\text{Case 6}}, \tag{5}$$

where $\mathbf{e}_r \equiv \mathbf{r}/r$ with $\mathbf{r} \equiv \mathbf{Y}^{(2)} - \mathbf{Y}^{(1)}$ and $r \equiv |\mathbf{r}|$. Note that each of the subproblems is essentially configured in two spatial dimensions.

For each case, three different separation ranges are considered: the short-range with $s \leqslant s_1$, the long-range with $s \geqslant s_2$, and the intermediate range $s_1 < s < s_2$. The two boundary locations, s_1 and s_2, separating the three ranges will be determined and optimized separately for each case.

2.1. Long-range interaction

First, we shall consider the long-range hydrodynamic interaction between two droplets. The FTS (Force–Torque–Stresslet) multipole expansion method [12] is applied. The expansion includes the monopole term representing the total force exerted by the particle on the fluid, and dipole terms. The symmetric dipole term is known as the stresslet and the antisymmetric dipole term is related to the torque exerted by the fluid on the particle [30]. Furthermore, the Faxen terms are also included to account for the effect of local variations in the Stokes flow on the surface of the particle relative to the velocity at the center. Summarizing, we used multipole expansion to evaluate the disturbance velocity field and Faxen law to calculate moments (force and torque) acting on the particles. In this FTS multipole expansion, the velocity at any point in the fluid is expressed as [12]

$$u_i(\mathbf{x}) = u_i^{\infty}(\mathbf{x}) + \sum_{\alpha=1}^{N_p} u_i^{(\alpha)}(\mathbf{x}, t), \tag{6}$$

with

$$u_i^{(\alpha)}(\mathbf{x}, t) = -\frac{1}{8\pi\mu}\left[\left(1 + \frac{1}{6}a_\alpha^2\nabla^2\right)J_{ij}F_j^{(\alpha)} + R_{ij}L_j^{(\alpha)} + \left(1 + \frac{1}{10}a_\alpha^2\nabla^2\right)K_{ijk}S_{jk}^{(\alpha)} + \cdots\right], \tag{7}$$

where N_p is the total number of interacting particles, $u_i^{\infty}(\mathbf{x})$ is the background air flow and $u_i^{(\alpha)}(\mathbf{x}, t)$ denotes the disturbance flow induced by the αth particle. In this paper, we only consider stagnant background flow so $u_i^{\infty}(\mathbf{x}) = \mathbf{0}$. In Eq. (7), J_{ij} is the free-space Green function or Stokeslet [30], R_{ij} is the rotlet defined as $R_{ij}(r) \equiv \frac{1}{4}\epsilon_{lkj}(\nabla_k J_{ij} - \nabla_j J_{ik}), L_j$ is torque, $K_{ijk} \equiv \frac{1}{2}(\nabla_k J_{ij} + \nabla_j J_{ik})$ and $S_{jk}^{(\alpha)}$ is the stresslet. We wish to point out a typo in [12]: the original Eq. (2.13) in their paper has a wrong sign before the last term. Eq. (7) includes this correction and is consistent with the expressions in Kim and Karrila ([30, pp. 27–28])

The Faxen formulae are then used to relate the velocity and angular velocity of the particles to the force, torque, and stresslet acting on fluid by the αth particle as follows [12]

$$\begin{aligned}
V_i^{(\alpha)} - u_i^{\infty} &= \frac{-F_i^{(\alpha)}}{6\pi\mu a} + \left(1 + \tfrac{1}{6}a^2\nabla^2\right)u_i'(\mathbf{x})\Big|_{\mathbf{x}=\mathbf{Y}^{(\alpha)}},\\
\Omega_i^{(\alpha)} - \Omega_i^{\infty} &= \frac{-L_i^{(\alpha)}}{8\pi\mu a^3} + \tfrac{1}{2}\epsilon_{ijk}\nabla_j u_k'(\mathbf{x})\Big|_{\mathbf{x}=\mathbf{Y}^{(\alpha)}},\\
-E_{ij}^{\infty} &= \frac{S_{ij}^{(\alpha)}}{\left(\frac{20}{3}\right)\pi\mu a^3} + \left(1 + \tfrac{a^2}{10}\nabla^2\right)e_{ij}'(\mathbf{x})\Big|_{\mathbf{x}=\mathbf{Y}^{(\alpha)}},
\end{aligned} \tag{8}$$

where $e_{ij}' \equiv \frac{1}{2}\left(\nabla_j u_i' + \nabla_i u_j'\right)$ is the summed rate of strain of the disturbance flow due to all other particles except the αth particle, namely, $u_i'(\mathbf{x}) = \sum_{k=1,k\neq\alpha}^{Np} u_i^{(k)}(\mathbf{x}, t); \Omega_i^{\infty}$ is half the vorticity of the background flow; and E_{ij}^{∞} is the rate of strain of the background flow.

Eqs. (7) and (8) together can be used to derive explicit expressions for the force and torque exerted on each particle. For each of the six subproblems, we have derived the specific results, see Eqs. (28)–(42) in Appendix B. For Cases 1 and 2, the system Eq. (8) reduces only to two independent equations and two unknowns (drag forces acting on the two particles). Torque is not present when two particles move along their line of centers. For Cases 3 to 6, the system consists of 6 coupled equations with 6 unknowns: two components each for force, torque and stresslet. These second-order or sixth-order linear systems are solved analytically by Gauss elimination.

2.2. Short-range interaction

For the short-range interaction, the FTS multipole expansion is no longer accurate. To handle accurately the lubrication forces all moments from the expansion, Eq. (7), must be included when applying Eq. (8). However, due to slow convergence at small separations, this approach is no longer effective or efficient. We turn instead to the leading-order lubrication expressions developed by JO84. The lubrication expansions seek the exact leading-order terms of the forces and torques, in terms of the nondimensional separation between surfaces of the two interacting particles defined as $\epsilon = s - 2$. Since the force and torque behave differently at short separations for different cases shown in Fig. 1, a part of our optimization strategy will involve a proper choice of the number of leading-order terms in each specific case, as illustrated below.

For Case 1, we include terms up to $O(\epsilon)$. The asymptotic expressions for force, $F^{(\alpha)}(\epsilon \to 0)$ exerted by the fluid on the particles α is given explicitly as [17]

$$\frac{F_{\text{Case 1}}^{(1)}}{6\pi\mu a_1 V_1} = -2g_{11}(\lambda)\epsilon^{-1} - 2g_{12}(\lambda)\ln(\epsilon^{-1}) - 2g_{13}(\lambda)\epsilon\ln(\epsilon^{-1}) - A_{11}^{X}(\lambda) + \frac{1}{2}(1+\lambda)A_{12}^{X}(\lambda) + O(\epsilon), \tag{9}$$

$$\frac{F^{(2)}_{\text{Case 1}}}{6\pi\mu a_2 V_2} = -2g_{11}(\lambda^{-1})\epsilon^{-1} - 2g_{12}(\lambda^{-1})\ln(\epsilon^{-1}) - 2g_{13}(\lambda^{-1})\epsilon\ln(\epsilon^{-1}) - A^X_{22}(\lambda) + \frac{1}{2}(1+\lambda^{-1})A^X_{21}(\lambda) + O(\epsilon), \tag{10}$$

where $\lambda \equiv a_2/a_1$ and

$$g_{11}(\lambda) = 2\lambda^2(1+\lambda)^{-3}, \tag{11}$$

$$g_{12}(\lambda) = \frac{1}{5}\lambda(1+7\lambda+\lambda^2)(1+\lambda)^{-3}, \tag{12}$$

$$g_{13}(\lambda) = \frac{1}{42}(1+18\lambda-29\lambda^2+18\lambda^3+\lambda^4)(1+\lambda)^{-3}. \tag{13}$$

The coefficients A^X_{ij} can be calculated based on the exact JO84 solution given in terms of infinite series summations. In general, each element of the series can be determined by using recurrence relations resulting from JO84's twin multipole expansion procedure. The notation and definition used for $A^X_{ij}(\lambda)$ in Eqs. (9) and (10) correspond exactly to those in JO84. In the present study, $A^X_{ij}(\lambda)$ was evaluated using the first 90 terms in the series which ensures accuracy of the computed $A^X_{ij}(\lambda)$ to within 10^{-5}. Table 1 lists the resulting values of A^X_{ij} as a function of the radius ratio, very similar to Table 2 in JO84 but with one more significant digit and 10 uniformly distributed λ values (instead of 6 nonuniformly distributed λ values in JO84).

For Case 3 the terms up to $O(\epsilon^2\ln\epsilon)$ were included to yield

$$\frac{F^{(1)}_{\text{Case 3}}}{6\pi\mu a_1 V_1} = -2g_{32}(\lambda)\ln(\epsilon^{-1}) - 2g_{33}(\lambda)\epsilon\ln(\epsilon^{-1}) - A^Y_{11}(\lambda) + \frac{1}{2}(1+\lambda)A^Y_{12}(\lambda) + O(\epsilon^2\ln\epsilon), \tag{14}$$

$$\frac{F^{(2)}_{\text{Case 3}}}{6\pi\mu a_2 V_2} = -2g_{32}(\lambda^{-1})\ln(\epsilon^{-1}) - 2g_{33}(\lambda)\epsilon\ln(\epsilon^{-1}) - A^Y_{22}(\lambda) + \frac{1}{2}(1+\lambda^{-1})A^Y_{21}(\lambda) + O(\epsilon^2\ln\epsilon), \tag{15}$$

where

$$g_{32}(\lambda) = \frac{4}{15}\lambda(1+7\lambda+\lambda^2)(1+\lambda)^{-3}, \tag{16}$$

$$g_{33}(\lambda) = \frac{1}{42}(1+18\lambda-29\lambda^2+18\lambda^3+\lambda^4)(1+\lambda)^{-3}. \tag{17}$$

Table 1
The coefficients A^X_{ij} and A^Y_{ij} as a function of radius ratio λ.

a_2/a_1	A^X_{11}	A^X_{12}, A^X_{21}	A^X_{22}	A^Y_{11}	A^Y_{12}, A^Y_{21}	A^Y_{22}
0.1	1.039750	−0.078658	0.468972	0.986950	−0.007227	0.243783
0.2	1.073058	−0.155578	0.578846	1.001530	−0.084398	0.593046
0.3	1.090218	−0.216321	0.668160	1.011807	−0.147208	0.755208
0.4	1.094047	−0.262369	0.744336	1.017390	−0.192820	0.845722
0.5	1.088061	−0.295804	0.808244	1.019317	−0.224570	0.900920
0.6	1.075317	−0.319110	0.861425	1.018493	−0.245990	0.936671
0.7	1.058191	−0.334545	0.905364	1.015575	−0.259846	0.960832
0.8	1.038411	−0.343952	0.941491	1.011025	−0.268160	0.977660
0.9	1.017193	−0.348791	0.971116	1.005178	−0.272397	0.989635
1.0	0.995376	−0.350197	0.995376	0.998285	−0.273623	0.998285

Table 2
Coefficients Q_i needed for the force asymptotic expression in Case 2 and Case 4.

a_2/a_1	$Q_2(\lambda)$	$Q_2(\lambda^{-1})$	$Q_4(\lambda)$	$Q_4(\lambda^{-1})$
0.1	−0.015668	0.168356	−0.030903	0.490716
0.2	−0.037520	0.229568	−0.025637	0.358856
0.3	−0.046451	0.226389	−0.011545	0.277367
0.4	−0.043268	0.215189	0.050740	0.219505
0.5	−0.034288	0.194070	0.020848	0.181503
0.6	−0.020521	0.163956	0.035453	0.153472
0.7	−0.032119	0.132347	0.049132	0.131321
0.8	0.016117	0.103277	0.062048	0.113345
0.9	0.036237	0.077929	0.074319	0.098503
1.0	0.056314	0.056313	0.086040	0.086040

Table 3
Short-range asymptotic expressions for forces exerted by the fluid on the droplets.

CASE	$\widetilde{F}_1 \equiv F_1/[6\pi\mu a_1 \mathbf{V}_1]$, $\widetilde{F}_2 \equiv F_2/[6\pi\mu a_2 \mathbf{V}_2]$	
1	$\widetilde{F}_1 = -2g_{11}(\lambda)\epsilon^{-1} - 2g_{12}(\lambda)\ln(\epsilon^{-1}) - 2g_{13}(\lambda)\epsilon\ln(\epsilon^{-1})$ $-A^X_{11}(\lambda) + \frac{1}{2}(1+\lambda)A^X_{12}(\lambda) + O(\epsilon)$	$g_{11}(\lambda) = 2\lambda^2(1+\lambda)^{-3}$
	$\widetilde{F}_2 = -2g_{11}(\lambda^{-1})\epsilon^{-1} - 2g_{12}(\lambda^{-1})\ln(\epsilon^{-1}) - 2g_{13}(\lambda^{-1})\epsilon\ln(\epsilon^{-1})$ $-A^X_{22}(\lambda) + \frac{1}{2}(1+\lambda^{-1})A^X_{21}(\lambda) + O(\epsilon)$	$g_{12}(\lambda) = \frac{1}{5}\lambda(1+7\lambda+\lambda^2)(1+\lambda)^{-3}$
		$g_{13}(\lambda) = \frac{1}{42}(1+18\lambda-29\lambda^2+18\lambda^3+\lambda^4)(1+\lambda)^{-3}$
2	$\widetilde{F}_1 = -A^X_{11}(\lambda) - \frac{1}{2}(1+\lambda)A^X_{12}(\lambda) - Q_2(\lambda)\epsilon + O(\epsilon^2)$	$A^X_{ij}(\lambda)$ coefficients are listed in Table 1
	$\widetilde{F}_2 = -A^X_{22}(\lambda) - \frac{1}{2}(1+\lambda^{-1})A^X_{21}(\lambda) - Q_2(\lambda^{-1})\epsilon + O(\epsilon^2)$	$Q_2(\lambda)$ coefficients are listed in Table 2
3	$\widetilde{F}_1 = -2g_{32}(\lambda)\ln(\epsilon^{-1}) - 2g_{33}(\lambda)\epsilon\ln(\epsilon^{-1}) - A^Y_{11}(\lambda) + \frac{1}{2}(1+\lambda)A^Y_{12}(\lambda) + O(\epsilon^2\ln(\epsilon))$	$g_{32}(\lambda) = \frac{4}{15}\lambda(2+\lambda+2\lambda^2)(1+\lambda)^{-3}$
	$\widetilde{F}_2 = -2g_{32}(\lambda^{-1})\ln(\epsilon^{-1}) - 2g_{33}(\lambda^{-1})\epsilon\ln(\epsilon^{-1}) - A^Y_{22}(\lambda) + \frac{1}{2}(1+\lambda^{-1})A^Y_{21}(\lambda) + O(\epsilon^2\ln(\epsilon))$	$g_{33}(\lambda) = \frac{2}{375}(16-45\lambda+58\lambda^2-45\lambda^3+16\lambda^4)(1+\lambda)^{-3}$
4	$\widetilde{F}_1 = -A^Y_{11}(\lambda) - \frac{1}{2}(1+\lambda)A^Y_{12}(\lambda) - Q_4(\lambda)\epsilon + O(\epsilon^2)$	$A^Y_{ij}(\lambda)$ coefficients are listed in Table 1
	$\widetilde{F}_2 = -A^Y_{22}(\lambda) - \frac{1}{2}(1+\lambda^{-1})A^Y_{21}(\lambda) - Q_4(\lambda^{-1})\epsilon + O(\epsilon^2)$	$Q_4(\lambda)$ coefficients are listed in Table 2
5	$\widetilde{F}_1 = B^5_1(\lambda) + h_2(\lambda)\ln\frac{s+2}{s-2} + h_3(\lambda)(1-4s^{-2})\ln\frac{s+2}{s-2} + 4h_3(\lambda)s^{-1} - \lambda^2 h_2(\lambda^{-1})\ln(1-4s^{-2})$ $-\lambda^2 h_3(\lambda^{-1})(1-4s^{-2})\ln(1-4s^{-2})$	$B^5_1(\lambda) = B^Y_{11}(\lambda) + \lambda^2 B^Y_{21}(\lambda)$
	$\widetilde{F}_2 = -[B^5_2(\lambda) + h_2(\lambda^{-1})\ln\frac{s+2}{s-2} + h_3(\lambda^{-1})(1-4s^{-2})\ln\frac{s+2}{s-2} + 4h_3(\lambda^{-1})s^{-1}$ $-\lambda^{-2}h_2(\lambda)\ln(1-4s^{-2}) - \lambda^{-2}h_3(\lambda)(1-4s^{-2})\ln(1-4s^{-2})]$	$B^5_1(\lambda) = B^Y_{22}(\lambda) + \lambda^{-2}B^Y_{12}(\lambda)$
		$B^6_1(\lambda) = B^Y_{11}(\lambda) - \lambda^2 B^Y_{21}(\lambda)$
		$B^6_2(\lambda) = B^Y_{22}(\lambda) - \lambda^{-2}B^Y_{12}(\lambda)$
6	$\widetilde{F}_1 = -[B^6_1(\lambda) + h_2(\lambda)\ln\frac{s+2}{s-2} + h_3(\lambda)(1-4s^{-2})\ln\frac{s+2}{s-2} + 4h_3(\lambda)s^{-1}$ $+\lambda^2 h_2(\lambda^{-1})\ln(1-4s^{-2}) + \lambda^2 h_3(\lambda^{-1})(1-4s^{-2})\ln(1-4s^{-2})]$	B^Y_{ij} coefficients are listed in Table 5
	$\widetilde{F}_2 = -[B^6_2(\lambda) + h_2(\lambda^{-1})\ln\frac{s+2}{s-2} + h_3(\lambda^{-1})(1-4s^{-2})\ln\frac{s+2}{s-2} + 4h_3(\lambda^{-1})s^{-1}$ $+\lambda^{-2}h_2(\lambda)\ln(1-4s^{-2}) + \lambda^{-2}h_3(\lambda)(1-4s^{-2})\ln(1-4s^{-2})]$	$h_2(\lambda) = -\frac{1}{5}\lambda(4+\lambda)(1+\lambda)^{-2}$
		$h_3(\lambda) = -\frac{1}{250}(32-33\lambda+83\lambda^2+43\lambda^3)(1+\lambda)^{-2}$

Note that the leading-order term for Case 3 is proportional to $\ln(\epsilon^{-1})$ instead of ϵ^{-1} in Case 1. Again our definition of $A^Y_{ij}(\lambda)$ corresponds exactly to the original definition in JO84. The above asymptotic expressions are similar for the two particles. The difference between the formulae defining force acting on the second particle from this acting on first one is the radius ratio λ, which is replaced by λ^{-1}, furthermore, A^X_{ij} is replaced by $A^X_{(3-i)(3-j)}$ and A^X_{ij} by $A^Y_{(3-i)(3-j)}$. The coefficients A^Y_{ij} were calculated in the same manner as A^X_{ij}, *i.e.*, based on the exact JO84 solution and are also listed in Table 1, as a function of radius ratio. Our values listed for A^Y_{ij} also extend those listed in Table 4 of JO84.

For Case 2 and Case 4, the leading-order term in the lubrication expansion reduces to a constant. In these cases, we found that the leading-order term alone is insufficient for the accurate computation of the collision efficiency. We therefore retain explicitly the $\mathcal{O}(\epsilon)$ term as

$$\frac{F^{(1)}_{\text{Case 2}}}{6\pi\mu a_1 V_1} = -A^X_{11}(\lambda) - \frac{1}{2}(1+\lambda)A^X_{12}(\lambda) - Q_2(\lambda)\epsilon + O(\epsilon^2), \tag{18}$$

$$\frac{F^{(2)}_{\text{Case 2}}}{6\pi\mu a_2 V_2} = -A^X_{22}(\lambda) - \frac{1}{2}(1+\lambda^{-1})A^X_{21}(\lambda) - Q_2(\lambda^{-1})\epsilon + O(\epsilon^2), \tag{19}$$

$$\frac{F^{(1)}_{\text{Case 4}}}{6\pi\mu a_1 V_1} = -A^Y_{11}(\lambda) - \frac{1}{2}(1+\lambda)A^Y_{12}(\lambda) - Q_4(\lambda)\epsilon + O(\epsilon^2), \tag{20}$$

$$\frac{F^{(2)}_{\text{Case 4}}}{6\pi\mu a_2 V_2} = -A^Y_{22}(\lambda) - \frac{1}{2}(1+\lambda^{-1})A^Y_{21}(\lambda) - Q_4(\lambda^{-1})\epsilon + O(\epsilon^2), \tag{21}$$

where the coefficients $Q_i(\lambda)$ were calculated again based on the exact JO84 solution and are listed in Table 2. Again the first 90 terms in the multipole expansion were used in our calculation to ensure accuracy of $Q_i(\lambda)$ to at least three significant digits. To our knowledge, these $\mathcal{O}(\epsilon)$ terms have not been explicitly calculated before. Because the coefficients $Q_i(\lambda)$ depend only on radius ratio and do not change with time, they can be calculated only once in advance. A polynomial fitting subroutine was used to obtain the value of $Q_i(\lambda)$ at any arbitrary λ from the tabulated values in Table 2.

The asymptotic relations for force in Cases 5 and 6 as well as torque for Cases 3 to 6 were taken directly from JO84 and these are shown in Tables 3 and 4. In all these equations the forces and the torques are analytical functions of the normalized separation $\epsilon = s - 2$ and multipole summations have already been performed.

Table 4
Short-range asymptotic expressions for torques acting on the particles.

CASE	$\widetilde{L}_1 \equiv L_1/[4\pi\mu a_1^2 \mathbf{V}_1 \times \mathbf{e}_r], \quad \widetilde{L}_2 \equiv L_2/[4\pi\mu a_2^2 \mathbf{V}_2 \times \mathbf{e}_r]$	
3	$\widetilde{L}_1 = -[B^Y_{11}(\lambda) + B^Y_{12}(\lambda) + h_2(\lambda)\ln\frac{s+2}{s-2} + h_3(\lambda)(1-4s^{-2})\ln\frac{s+2}{s-2} + 4h_3(\lambda)s^{-1} - h_2(\lambda)\ln(1-4s^{-2}) - h_3(\lambda)(1-4s^{-2})\ln(1-4s^{-2})]$	$h_2(\lambda) = -\frac{1}{5}\lambda(4+\lambda)(1+\lambda)^{-2}$
	$\widetilde{L}_2 = B^Y_{22}(\lambda) + B^Y_{21}(\lambda) + h_2(\lambda^{-1})\ln\frac{s+2}{s-2} + h_3(\lambda^{-1})(1-4s^{-2})\ln\frac{s+2}{s-2} + 4h_3(\lambda^{-1})s^{-1} - h_2(\lambda^{-1})\ln(1-4s^{-2}) - h_3(\lambda^{-1})(1-4s^{-2})\ln(1-4s^{-2})$	$h_3(\lambda) = -\frac{1}{250}(32-33\lambda+83\lambda^2+43\lambda^3)(1+\lambda)^{-2}$
4	$\widetilde{L}_1 = B^Y_{11}(\lambda) - B^Y_{12}(\lambda) + h_2(\lambda)\ln\frac{s+2}{s-2} + h_3(\lambda)(1-4s^{-2})\ln\frac{s+2}{s-2} + 4h_3(\lambda)s^{-1} + h_2(\lambda)\ln(1-4s^{-2}) + h_3(\lambda)(1-4s^{-2})\ln(1-4s^{-2})$	$B^Y_{ij}(\lambda)$ coefficients are listed in Table 5
	$\widetilde{L}_2 = -[B^Y_{22}(\lambda) - B^Y_{21}(\lambda) + h_2(\lambda^{-1})\ln\frac{s+2}{s-2} + h_3(\lambda^{-1})(1-4s^{-2})\ln\frac{s+2}{s-2} + 4h_3(\lambda^{-1})s^{-1} + h_2(\lambda^{-1})\ln(1-4s^{-2}) + h_3(\lambda^{-1})(1-4s^{-2})\ln(1-4s^{-2})]$	
CASE	$\widetilde{L}_1 \equiv L_1/[8\pi\mu a_1^3 \mathbf{\Omega}_1], \quad \widetilde{L}_2 \equiv L_2/[8\pi\mu a_2^3 \mathbf{\Omega}_2]$	
5	$\widetilde{L}_1 = -[C^Y_{11}(\lambda) - q_2(\lambda)\ln(1-4s^{-2}) - q_3(\lambda)(1-4s^{-2})\ln(1-4s^{-2}) + 1 + q_4(\lambda)\ln\frac{s+2}{s-2} + q_5(\lambda)(1-4s^{-2})\ln\frac{s+2}{s-2} + 4q_5(\lambda)s^{-1} + C^Y_{12}(\lambda)]$	$q_2(\lambda) = \frac{2}{5}\lambda(1+\lambda)^{-1}$
	$\widetilde{L}_2 = -[C^Y_{22}(\lambda) - q_2(\lambda^{-1})\ln(1-4s^{-2}) - q_3(\lambda^{-1})(1-4s^{-2})\ln(1-4s^{-2}) + 1 + q_4(\lambda^{-1})\ln\frac{s+2}{s-2} + q_5(\lambda^{-1})(1-4s^{-2})\ln\frac{s+2}{s-2} + 4q_5(\lambda^{-1})s^{-1} + C^Y_{21}(\lambda)]$	$q_3(\lambda) = \frac{1}{125}(8+6\lambda+33\lambda^2)(1+\lambda)^{-1}$
		$q_4(\lambda) = \frac{4}{5}\lambda^2(1+\lambda)^{-4}$
		$q_5(\lambda) = \frac{4}{125}\lambda(43-24\lambda+43\lambda^2)\cdot(1+\lambda)^{-4}$
6	$\widetilde{L}_1 = -[C^Y_{11}(\lambda) - q_2(\lambda)\ln(1-4s^{-2}) - q_3(\lambda)(1-4s^{-2})\ln(1-4s^{-2}) + 1 - q_4(\lambda)\ln\frac{s+2}{s-2} - q_5(\lambda)(1-4s^{-2})\ln\frac{s+2}{s-2} - 4q_5(\lambda)s^{-1} - C^Y_{12}(\lambda)]$	$C^Y_{ij}(\lambda)$ coefficients are listed in Table 5
	$\widetilde{L}_2 = -[C^Y_{22}(\lambda) - q_2(\lambda^{-1})\ln(1-4s^{-2}) - q_3(\lambda^{-1})(1-4s^{-2})\ln(1-4s^{-2}) + 1 - q_4(\lambda^{-1})\ln\frac{s+2}{s-2} - q_5(\lambda^{-1})(1-4s^{-2})\ln\frac{s+2}{s-2} - 4q_5(\lambda^{-1})s^{-1} - C^Y_{21}(\lambda)]$	

Table 5
The coefficients $B^Y_{ij}(\lambda)$ and $C^Y_{ij}(\lambda)$ for $0.1 < \lambda < 1$.

a_2/a_1	B^Y_{11}	B^Y_{12}	B^Y_{21}	B^Y_{22}
0.1	0.330265	0.016913	0.646628	4.449282
0.2	0.376433	−0.011555	0.440554	2.588261
0.3	0.429274	−0.032189	0.310820	1.923686
0.4	0.486368	−0.043033	0.220266	1.568563
0.5	0.545331	−0.045944	0.154349	1.342071
0.6	0.604752	−0.042874	0.105264	1.182778
0.7	0.663828	−0.035462	0.068201	1.063726
0.8	0.722115	−0.024980	0.039958	0.971003
0.9	0.779385	−0.012373	0.018308	0.896601
1.0	0.835540	0.001660	0.001660	0.835540
a_2/a_1	C^Y_{11}	C^Y_{12}	C^Y_{21}	C^Y_{22}
0.1	−0.031694	−0.211484	1.201267	−1.191910
0.2	−0.057327	−0.330059	0.683680	−0.885984
0.3	−0.087413	−0.394502	0.349170	−0.714592
0.4	−0.119187	−0.425773	0.128861	−0.599753
0.5	−0.151107	−0.435849	−0.023016	−0.516115
0.6	−0.182422	−0.431912	−0.131217	−0.452094
0.7	−0.212790	−0.418473	−0.210171	−0.401376
0.8	−0.242071	−0.398479	−0.268791	−0.360161
0.9	−0.270221	−0.373923	−0.312842	−0.326004
1.0	−0.297248	−0.346191	−0.346191	−0.297248

The coefficients B^Y_{ij} involved in Cases 4 to 6 (see Tables 3 and 4) in present study do not correspond to their original definition B^Y_{ijJO} used in JO84. We kept the same notation only for the coefficients with repeating indexes $B^Y_{ii} = B^Y_{iiJO}$. For the coefficients with different indices the following modification was done: $B^Y_{12} = -\frac{1}{4}(1+\lambda)^2 B^Y_{12JO} - 2h_2(\lambda)\ln 2 - 2h_3(\lambda)$ and $B^Y_{21} = -\frac{1}{4}(1+\lambda^{-1})^2 B^Y_{21JO} - 2h_2(\lambda^{-1})\ln 2 - 2h_3(\lambda^{-1})$, where the function $h_2(\lambda) = -\frac{1}{5}\lambda(4+\lambda)(1+\lambda)^{-2}$ and $h_3(\lambda) = -\frac{1}{250}(32-33\lambda+83\lambda^2+43\lambda^3)(1+\lambda)^{-2}$. We have also changed the definition of C^Y_{ij} coefficients involved in torque calculation due to rotating spheres. The new definition of C^Y_{ij} is related to the original one in JO84 as follows: $C^Y_{ii} = C^Y_{iiJO} - 1, C^Y_{ij} = C^Y_{ijJO} - 2h_4\ln 2 - 2h_5$, where $h_4(\lambda) = \frac{4}{5}\lambda^2(1+\lambda)^{-4}$ and $h_5(\lambda) = \frac{4}{125}\lambda(43-24\lambda+43\lambda^2)(1+\lambda)^{-4}$.

In summary, Tables 1–5 include all details necessary for obtaining correct and accurate asymptotic results for forces and torques acting on the particles. In compiling and calculating the above details, a few typographic errors and inconsistencies were found in JO84. These are listed in Appendix C as identifying these could require a significant effort.

2.3. Interaction at intermediate separations

Currently there is no efficient method to accurately describe the interaction forces and torques in the intermediate separation range. The method of reflections [28,31] or multipole expansion [30] requires more and more terms as the separation distance between particles is decreased. Meanwhile, the short-range asymptotic expansions discussed in the last subsection become inaccurate when $\epsilon \to 1$. Here we propose an efficient method based on a polynomial fitting approach.

Table 6
Polynomial forms used to fit force and torque in the intermediate-separation range.

CASE	$\widetilde{F}$ – force normalized by $6\pi\mu a_i \mathbf{V_i}$	$\widetilde{L}$ – torque normalized by $8\pi\mu a_i^2 \mathbf{\Omega_i}$
1	$\ln(\widetilde{F}) = A + B\ln(\epsilon) + C\ln^2(\epsilon) + D\ln^3(\epsilon)$	–
2	$\widetilde{F} = A + B\epsilon + C\epsilon^2 + D\epsilon^3$	–
3	$\widetilde{F} = A + B\ln(\epsilon) + C\ln^2(\epsilon) + D\ln^3(\epsilon)$	$\ln(\widetilde{L}) = A + B\ln(\epsilon) + C\ln^2(\epsilon) + D\ln^3(\epsilon)$
4	$\widetilde{F} = A + B\epsilon + C\epsilon^2 + D\epsilon^3$	$\ln(\widetilde{L}) = A + B\ln(\epsilon) + C\ln^2(\epsilon) + D\ln^3(\epsilon)$
5	$\ln(\widetilde{F}) = A + B\ln(\epsilon) + C\ln^2(\epsilon) + D\ln^3(\epsilon)$	$\ln(\widetilde{L}) = A + B\ln(\epsilon) + C\ln^2(\epsilon) + D\ln^3(\epsilon)$
6	$\ln(\widetilde{F}) = A + B\ln(\epsilon) + C\ln^2(\epsilon) + D\ln^3(\epsilon)$	$\ln(\widetilde{L}) = A + B\ln(\epsilon) + C\ln^2(\epsilon) + D\ln^3(\epsilon)$

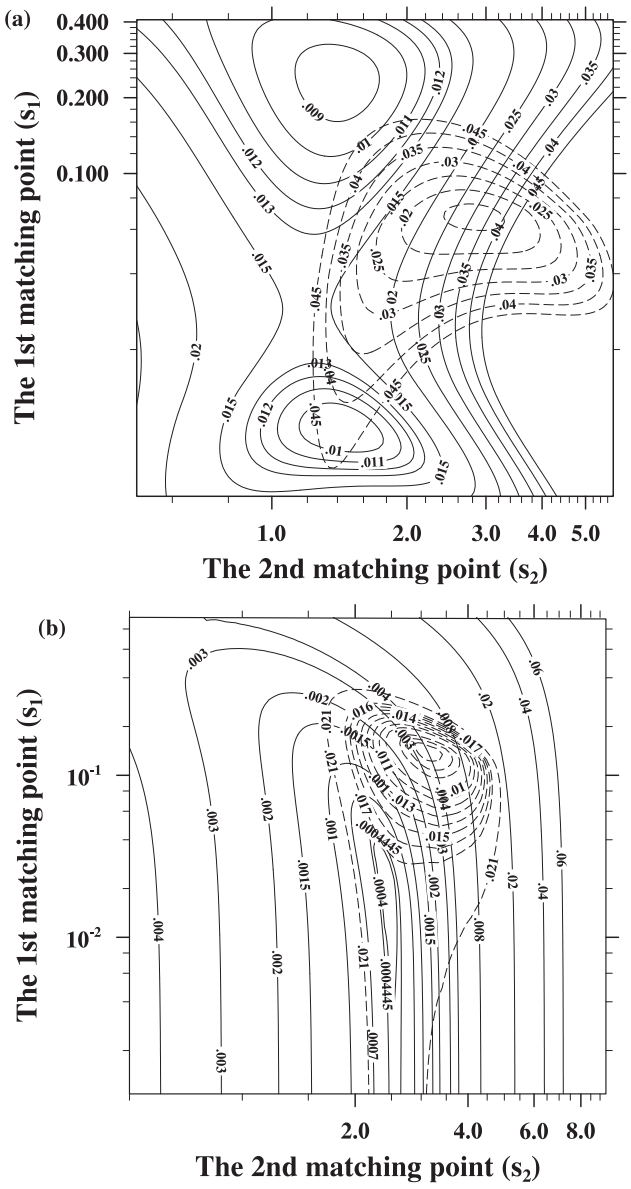

Fig. 2. (a) Contour plot of the cumulative relative error for Case 1 at $a_2/a_1 = 0.1$. The solid lines corresponds to the larger particle (LD), the dashed lines for the smaller particle (SD). It appears that the error surface for the larger particle contains two minimum points but the one with the smaller cumulative error is selected. (b) Cumulative relative error for Case 2 at $a_2/a_1 = 0.2$.

The basic idea is to construct a third-order polynomial function that matches, on the left boundary of the intermediate-separation range, both the value and local gradient with the short-range asymptotic expression at some small s, say $s = s_1$, and, at the same time, on the right boundary of the intermediate-separation range, the value and gradient provided by the FTS multipole expansion at another value of s, say $s = s_2$. The intermediate-separation range is then defined as $s_1 \leqslant s \leqslant s_2$. It is assumed that the short-range asymptotic expression is accurate for $s < s_1$ whereas the FTS expansion is accurate for $s > s_2$. Conceptually, this matching is straightforward, but its optimization depends on the choice of s_1 and s_2 for each case, as well as the optimal selection of appropriate coordinates (*i.e.*, linear vs. logarithmic) for each case. These are described next.

Consider, for example, Case 1. We found the best option is to use logarithmic coordinates for both the interaction force and the separation. Namely, the third-order polynomial function is written as

$$\ln(\widetilde{F}) = A + B\ln\epsilon + C\ln^2\epsilon + D\ln^3\epsilon, \tag{22}$$

where $\widetilde{F} \equiv F/(6\pi\mu a_i V_i)$. Note that this form is applied typically to the range of $\mathcal{O}(0.01) < \epsilon < \mathcal{O}(2.0)$ or a range of $\ln\epsilon$ from roughly -5.0 to 0.5, it can reasonably reproduce the short-range limit of $\widetilde{F} \propto \epsilon^{-1}$ provided that the magnitudes of C and D are small relative to the magnitudes of A and B coefficients, and at the same time, accommodates the long-range limit of $\widetilde{F} \to$ constant. The above form should not be viewed as a series expansion as it does not converge when $\epsilon \to 0$. The idea is to just construct a third-order polynomial with optimal coordinates for $\widetilde{F}$ and ϵ. By trial and error in minimizing a cumulative relative error to be introduced in Section 3.1, we concluded that the above form works the best for this case.

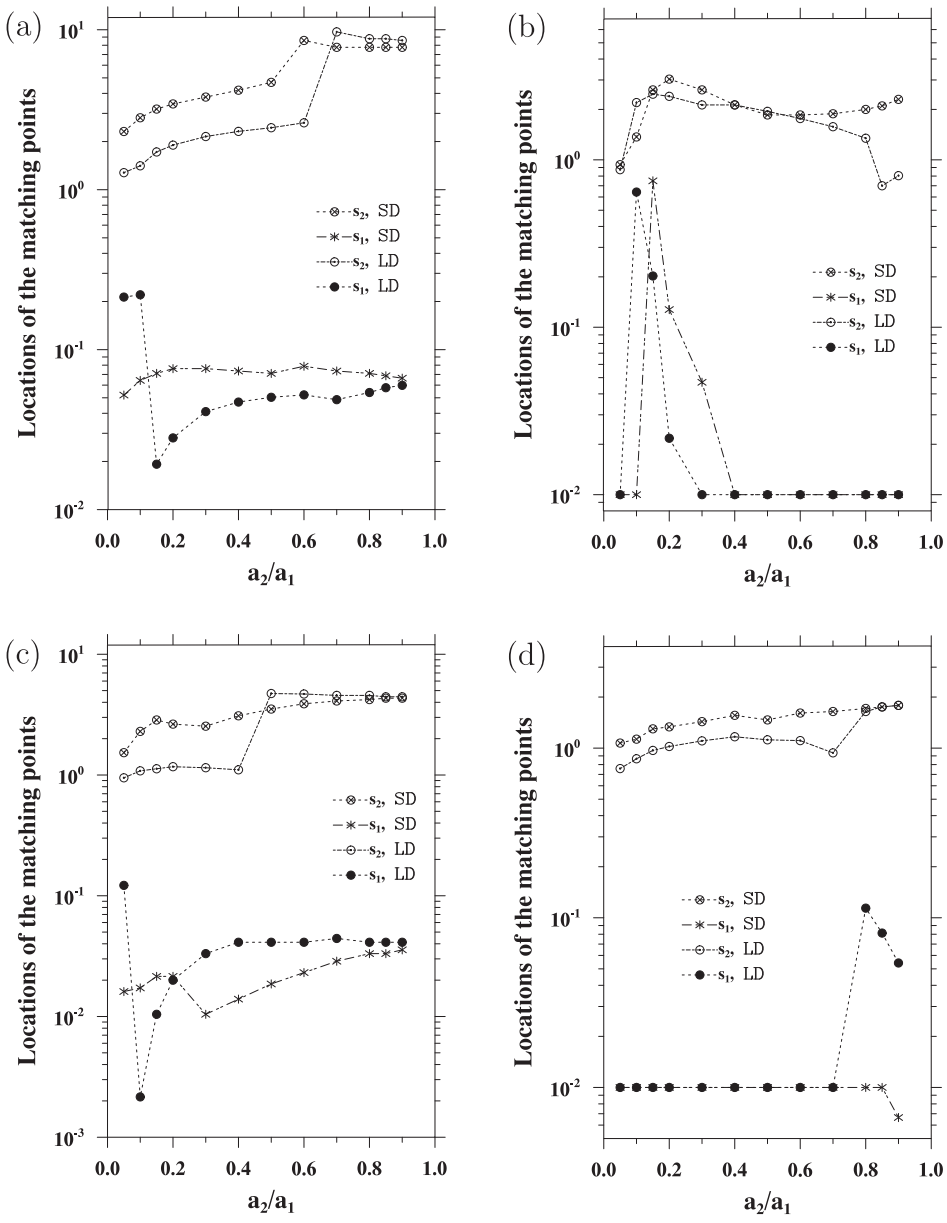

Fig. 3. Optimal matching locations for Case 1 (a), Case 2 (b), Case 3 (c), Case 4 (d). The four lines correspond to the two matching locations s_1 and s_2 for larger (LD) and smaller (SD) droplets.

For Case 2 and Case 4, we instead employed the following polynomial fitting:

$$\widetilde{F} = A + B\epsilon + C\epsilon^2 + D\epsilon^3. \tag{23}$$

Again the leading-order term of this form conforms with the asymptotic behavior shown in Eqs. (18)–(21).

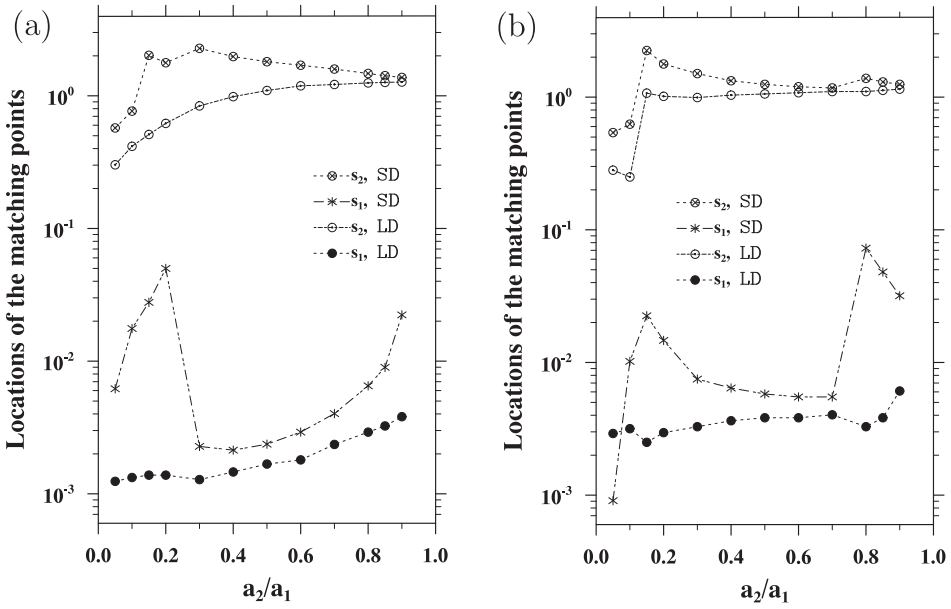

Fig. 4. Optimal matching locations for Case 5 (a) and Case 6 (b).

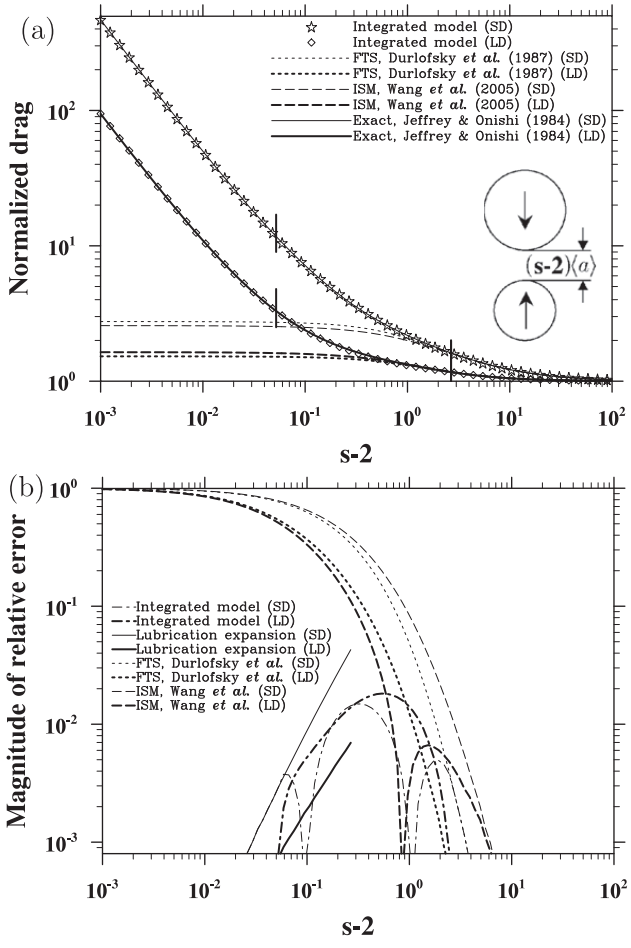

Fig. 5. (a) Normalized drag force for Case 1 with $\lambda = 0.2$. The matching locations s_1 and s_2 are indicated by the short vertical lines. (b) The local relative error.

Similarly, considering the asymptotic expressions shown in Eqs. (14) and (15), the best form for Case 3 was found to be

$$\widetilde{F} = A + B\ln\epsilon + C\ln^2\epsilon + D\ln^3\epsilon. \tag{24}$$

Other polynomial forms used for force representation in Cases 5 and 6 and for torque representation in Cases 3 to 6 are compiled in Table 6.

When the polynomial form was chosen, the locations of the matching points s_1 and s_2 were found by the minimizing the difference between the exact force representation and our integrated approach. This optimization step will be discussed next.

3. Results and discussion

3.1. Optimization of s_1 and s_2

The optimization of s_1 and s_2 was performed by minimizing a cumulative relative error (CRE) between our efficient treatment, F_{Approx}, and the full solution given by JO84, F_{Exact}. For Cases 1 to 4, the cumulative relative error is defined by integrating the relative error of our representation as

$$\text{CRE} \equiv \int_{\epsilon=0.001}^{\epsilon=100} \frac{|F_{\text{Approx}} - F_{\text{Exact}}|}{|F_{\text{Exact}}|} d\ln\epsilon, \tag{25}$$

where the lower and upper limits fall well within the short-range and long-range interactions, respectively. In Cases 5 and 6 the same cumulative error was used but forces were replaced by torques. This treatment is justified, because torques have stronger influence on particle-particle interaction in Cases 5 and 6. In fact, for Cases 5 and 6, forces are weak for $\epsilon < 1$ and are essentially zero when $\epsilon \sim 1$. Because in each case particles move either with the same velocity $V^{(1)} = \mp V^{(2)}$ or the same angular velocity $\Omega^{(1)} = \mp\Omega^{(2)}$, the optimization procedure does not involve velocity ratio or angular velocity ratio. This is another benefit for the decomposition shown in Fig. 1.

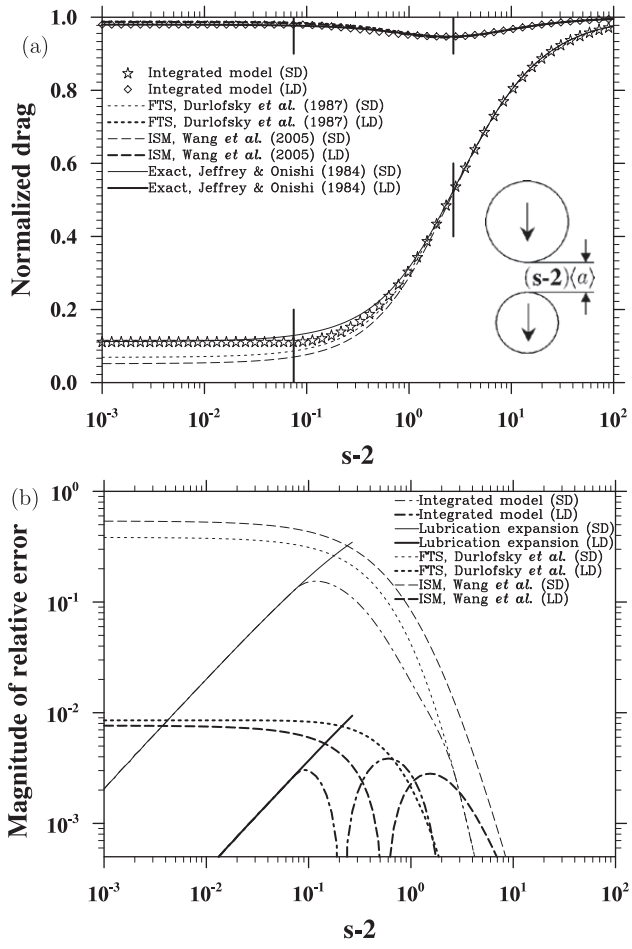

Fig. 6. (a) Normalized drag force and (b) magnitude of relative error for Case 2 with $\lambda = 0.2$.

The optimization process proceeds as follows. First, initial estimates for s_1 and s_2 are made, following the study of Davis [21]. The estimates are then refined by the resulting cumulative error as s_1 and s_2 are varied ($s_1 < s_2$). Fig. 2 shows two-dimensional contour plots of CRE as a function of s_1 and s_2, for two specific cases. For each particle in the pair, a CRE surface can be constructed. The optimal value of s_1 and s_2 corresponds to the minimum value of the CRE surface, and Fig. 2 demonstrates that an optimal location for (s_1,s_2) can usually be identified for each particle in the pair. If there are multiple minima, e.g., Fig. 2(a), the point on the CRE surface with the lowest CRE is chosen. Fig. 2 also shows that at the optimal location, CRE is typically less than 0.01.

This optimal location in the (s_1,s_2) plane can be different for the larger and smaller droplets, as shown in Figs. 3 and 4 for the six different cases. In the legends, LD stands for larger droplet in the pair and SD for smaller droplet. When multiple minima of the CRE surface exist, the optimal location could switch suddenly from one CRE minimum to another, leading to occasionally a rapid change of optimal s_i for some ranges of a_2/a_1 (Figs. 3 and 4). Fortunately, the overall trends as a function of the radius ratio are similar. As the best compromise, the average values of s_i for the two droplets were taken to be the final optimal s_i. Figs. 3 and 4 indicate that the optimal value for s_1 is typically between 0.01 and 0.05, while the optimal s_2 falls in between 1.0 and 5. These optimal s_1 and s_2 were tabulated as a function of a_2/a_1 to complete our representation.

3.2. Accuracy of force representation

Once the matching locations, s_1 and s_2, are determined, it is straightforward to determine the coefficients A, B, C, D in Table 6 using the 2 matching equations at s_1 and the 2 matching equations at s_2. This amounts to solving a 4th-oder linear system. At this point, we have a smoothly connected, integrated model for force and torque representations by combining the short-range asymptotic expansion for $s < s_1$, the third-oder polynomial fitting for $s_1 \leqslant s \leqslant s_2$, and the FTS approximation for $s > s_2$. Below we shall examine the accuracy of this integrated model.

Fig. 5(a) compares the predicted normalized drags of our integrated model with the exact JO84 solutions, for Case 1 at $\lambda = 0.2$. The matching locations, s_1 and s_2, are indicated by short vertical lines. Our model predicts well the drags on both larger and smaller droplets. Fig. 5(b) shows the local relative error as a function of the normalized separation. The FTS

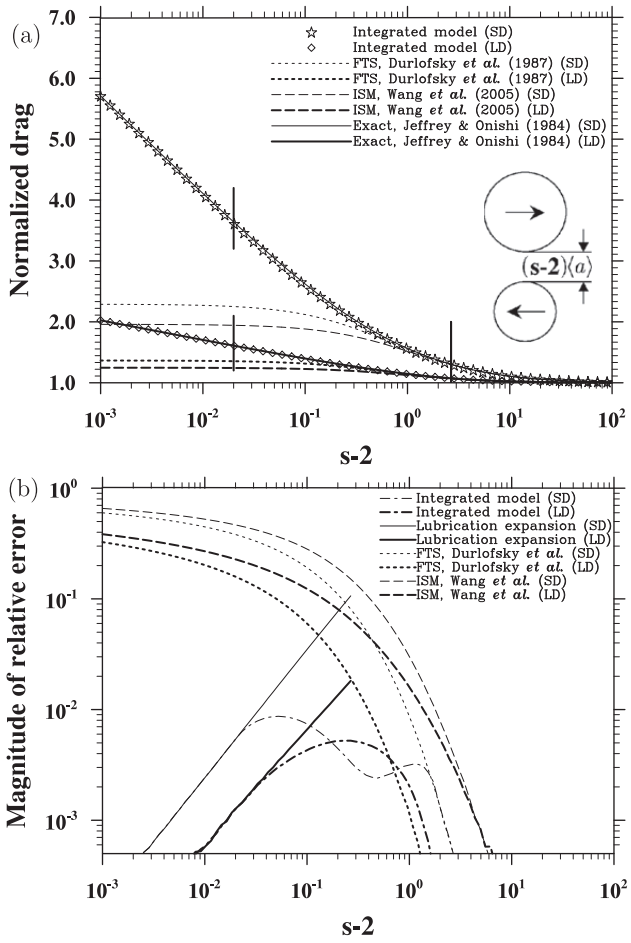

Fig. 7. (a) Normalized drag force and (b) magnitude of relative error for Case 3 with $\lambda = 0.2$.

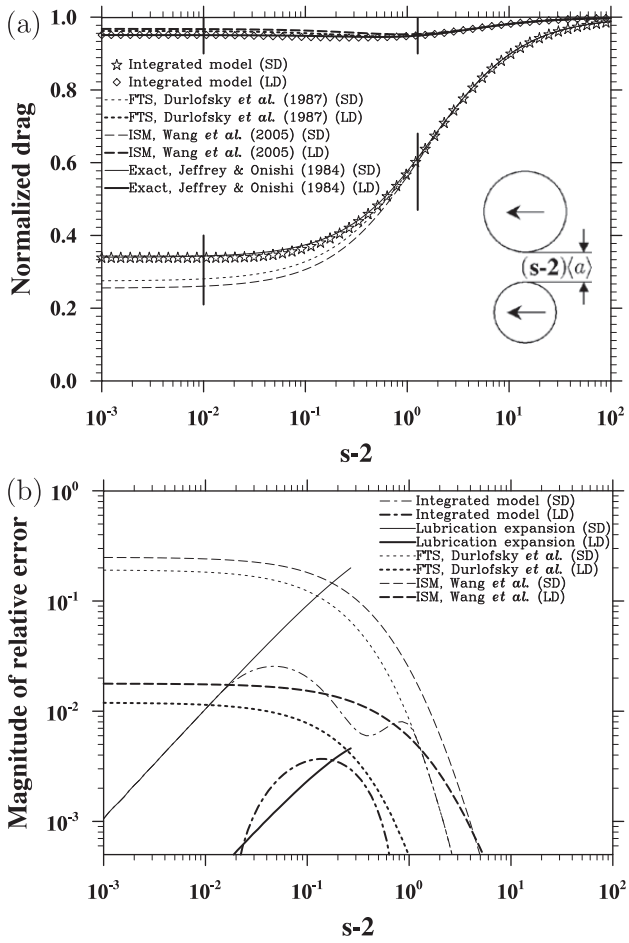

Fig. 8. (a) Normalized drag force and (b) magnitude of relative error for Case 4 with $\lambda = 0.2$.

approximation is only accurate for $\epsilon > 2.0$, while the short-range expansions are acceptable for $\epsilon < 0.1$. The optimal matching in our model performs well for the intermediate separations, with a maximum relative error of only about 1 to 2%. Also shown are the results of the improved superposition method (ISM) from [8], which are quite similar to the FTS results. Interestingly, ISM is less accurate than FTS when predicting the drag on the smaller droplet, but becomes more accurate when predicting the drag on the larger droplet. Clearly, our integrated model performs much better than FTS and ISM for $\epsilon < 0.5$ and becomes superior as $\epsilon \to 0$ since the exact short-range solutions are properly recovered.

Results for Cases 2, 3, and 4 at the same λ are shown in Figs. 6–8, respectively. They are used to demonstrate that our integrated model can handle different interaction configurations. The identical line styles and symbols are used in the figures: the solid lines correspond to the results based on the exact force representation of JO84, the symbols represent the results from our integrated model, and the two dashed lines denote results using FTS and ISM. In all these cases, an excellent agreement is shown between our integrated model and the exact solution. The typical local relative error of our integrated model is 2% or less, except for Case 2 in Fig. 6 where the relative error for the smaller droplet could reach 10% in the intermediate separation region.

In Case 1 and Case 2, torque is not present so the optimization of the matching locations s_1 and s_2 is based on the force representation only. In Case 3 and Case 4, the shear flow induces particle rotation so both torque and force must be calculated. Here we decided to still determine the optimal matching locations based on the minimization the cumulative error of the calculated drag force for our integrated model, and then use these as the matching locations for torque calculations. This choice was made since the torques become insignificant for a separation larger than the average size of the droplets while the drag forces are more persistent for intermediate to large separations.

For Case 5 and Case 6, torques represent the dominant interaction and therefore the optimal matching locations s_1 and s_2 are determined based on a minimization of the cumulative error on the torque rather than the force. In these two cases, drag forces are negligible at large separations but torques remain nonzero. Figs. 9 and 10 compare normalized torques and relative errors for $\lambda = 0.5$. Interestingly, for Case 6, the torque magnitude on the smaller droplet is non-monotonic with changing separation distance due to the counter-acting effect from the larger droplet at intermediate distance. At very short separations, the torques increase linearly with $\ln(s-2)$, consistent with the lubrication theory. The maximum relative error for the larger droplet is less than 1% and that for the smaller droplet does not exceed 5%.

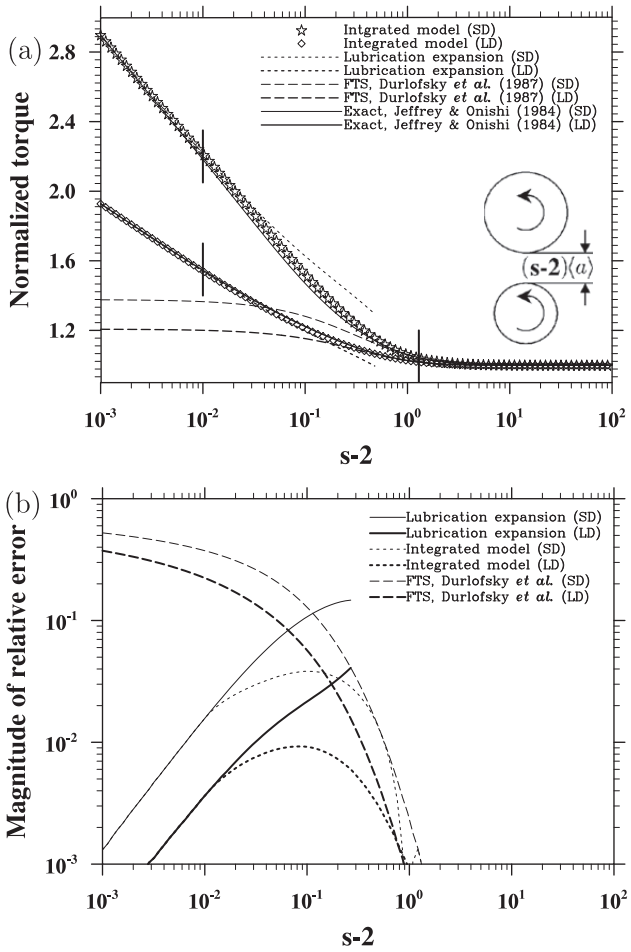

Fig. 9. (a) Normalized torque and (b) magnitude of relative error for Case 5 with $\lambda = 0.5$.

3.3. Collision efficiency

We shall now consider how well our integrated model predicts the collision efficiency. Since we consider here the collision efficiency for the stagnant background flow case, the collision efficiencies were determined by the far field off-center horizontal separation for the grazing trajectories with an efficient midpoint iteration algorithm following [8]. For time discretization we employed the fifth-order Runge–Kutta scheme with adaptive time step size. A coalescence event of two colliding droplets[1] is assumed to occur if the minimum gap between the surface of two droplets falls bellow $0.001a_1$, following the studies of Hocking and Jonas [20] and Davis and Sartor [19]. We will refer to this as the finite-gap model. This treatment may be viewed as a simplified model for the van der Waals interaction, without introducing any additional physical time scale. To demonstrate the accuracy of our method in computing the collision efficiency, we compare in Fig. 11 the resulting collision efficiency using our integrated force/torque representation to that obtained with exact force/torque solutions of JO84. In the exact treatment, typically 90 terms in the expansion of JO84 were used to ensure accuracy of the results, namely, further increase of the number of terms in the exact solutions does not alter the results shown. The curves marked with NR (*i.e.*, no rotation) represent results obtained when the angular velocities of the droplets were set to zero, namely, the rotational motion was not solved. The purpose is to examine how much change in collision efficiency is caused by the rotational motion of droplets. Several observations can be made from Fig. 11. First, for both non-rotating and rotating droplets, the relative error in the collision efficiency is found to be less than 5% for most cases, as shown in Tables 7 and 8. Even for the more difficult cases of very small and very large radius ratios our model prediction is within 15% of the exact value. The second observation is that the rotational motion does not significantly affect collision efficiency. The rotational effect is more noticeable for smaller droplets ($a_1 \leqslant 20$ μm), and tends to reduce the collision efficiency. Since only translational relative motion of droplets can directly contribute to the collision efficiency this implies that the rotational motion can slightly increase the near-field interaction force, through Case 5 and Case 6 shown in Fig. 1. The additional interaction forces related to Case 5 and Case 6 are found to be typically $\mathcal{O}(10^3)$ times smaller than the interaction forces from Cases 1 to 4.

[1] Sometime the term *collection efficiency* is used instead when a coalescence mechanism is considered in the detection of collision–coalescence events, such as the finite-gap model used here or inclusion of the van der Waals force, as described later in this section.

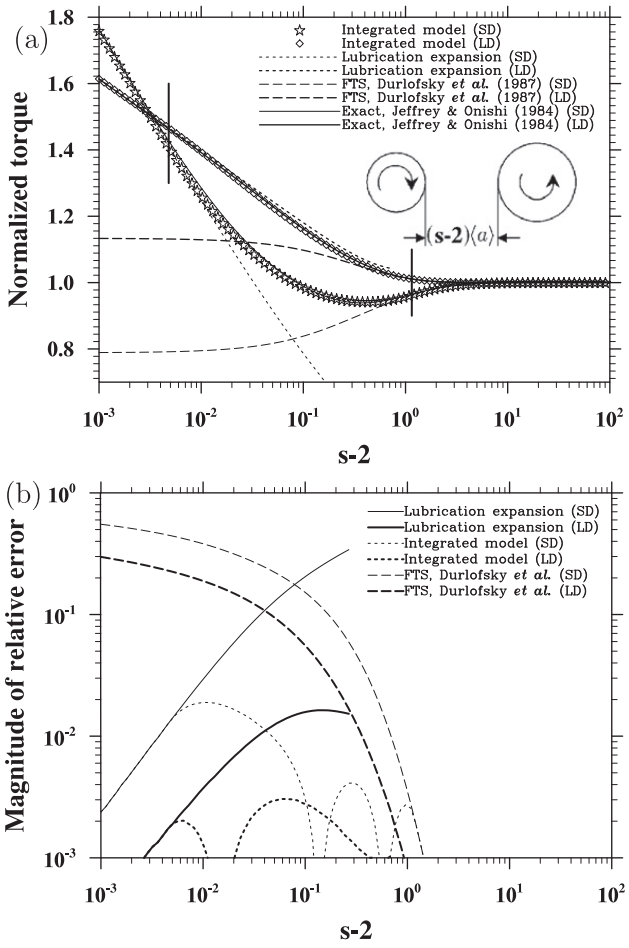

Fig. 10. (a) Normalized torque and (b) magnitude of relative error for Case 6 with $\lambda = 0.5$.

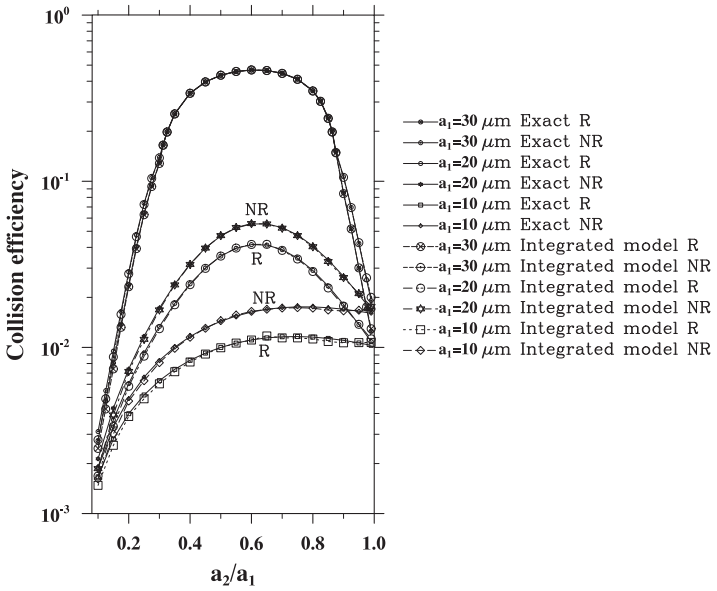

Fig. 11. Validation of our integrated model by comparing the collision efficiency based on our approximate force/torque formulation to the collision efficiency obtained using the exact force/torque solution of JO84.

It is noted that our method is computationally much more efficient than the exact treatment of JO84. For both approaches quantitative comparison of calculation efficiency were done in several tests. In these tests collision efficiency was calculated for $a_1 = 20$ μm and $\lambda = 0.5$. Rotation was taken into account. The calculation of collision efficiency using our model was

Table 7
Calculated collision efficiencies compared with those based on the exact JO84 solution. A small gap of $0.001a_1$ was used for coalescence detection. The rotational degrees of freedom were omitted. R.E. here denotes the relative error.

a_2/a_1	Drop radius a_1 (μm)								
	10 μm			20 μm			30 μm		
	Exact	Our approach	R.E. %	Exact	Our approach	R.E. %	Exact	Our approach	R.E. %
0.10	0.001869	0.001616	13.54	0.002135	0.001863	12.74	0.003113	0.002780	10.70
0.15	0.003321	0.003010	9.36	0.004313	0.003922	9.07	0.009494	0.008761	7.72
0.20	0.004920	0.004754	3.37	0.007407	0.007169	3.21	0.028463	0.027731	2.57
0.25	0.006623	0.006298	4.91	0.011667	0.011182	4.16	0.073658	0.072471	1.61
0.30	0.008349	0.008089	3.11	0.017227	0.016817	2.38	0.139105	0.138226	0.63
0.35	0.010033	0.009861	1.71	0.024042	0.023775	1.11	0.255019	0.254594	0.17
0.40	0.011624	0.011499	1.08	0.031774	0.031579	0.61	0.339223	0.338925	0.09
0.45	0.013082	0.013030	0.40	0.039713	0.039619	0.24	0.396614	0.396536	0.02
0.50	0.014367	0.014480	0.79	0.046899	0.047071	0.37	0.434754	0.435145	0.09
0.55	0.015453	0.015655	1.31	0.052353	0.052694	0.65	0.457710	0.458310	0.13
0.60	0.016318	0.016467	0.91	0.055310	0.055594	0.51	0.467472	0.467979	0.11
0.65	0.016952	0.016956	0.02	0.055379	0.055328	0.09	0.464437	0.464311	0.03
0.70	0.017357	0.017237	0.69	0.052603	0.052212	0.74	0.447343	0.446298	0.23
0.75	0.017544	0.017338	1.17	0.047463	0.047071	0.83	0.412458	0.411254	0.29
0.80	0.017526	0.017223	1.73	0.040797	0.040347	1.10	0.351131	0.349906	0.35
0.85	0.017330	0.016764	3.27	0.033604	0.032878	2.16	0.241625	0.239495	0.88
0.90	0.016978	0.016578	2.36	0.026768	0.026304	1.73	0.106436	0.105516	0.86
0.95	0.016500	0.016736	1.43	0.020804	0.021064	1.25	0.042337	0.042714	0.89
0.99	0.016045	0.016873	5.16	0.016797	0.017637	5.00	0.019134	0.020015	4.60

Table 8
Calculated collision efficiencies (rotation included) compared with those based on the exact JO84 solution. A small gap of $0.001a_1$ was used for coalescence detection.

a_2/a_1	Drop radius a_1 (μm)								
	10 μm			20 μm			30 μm		
	Exact	Our approach	R.E. %	Exact	Our approach	R.E. %	Exact	Our approach	R.E. %
0.10	0.001663	0.001478	11.12	0.001896	0.001682	11.29	0.002751	0.002465	10.40
0.15	0.002814	0.002575	8.49	0.003663	0.003342	8.76	0.008063	0.007421	7.96
0.20	0.003990	0.003841	3.73	0.006055	0.005833	3.67	0.023860	0.023170	2.89
0.25	0.005170	0.004907	5.09	0.009256	0.008854	4.34	0.064005	0.062898	1.73
0.30	0.006311	0.006036	4.36	0.013371	0.012958	3.09	0.129159	0.127953	0.93
0.35	0.007382	0.007141	3.26	0.018399	0.018059	1.85	0.254438	0.253980	0.18
0.40	0.008364	0.008167	2.36	0.024129	0.023863	1.10	0.338588	0.338267	0.09
0.45	0.009242	0.009120	1.32	0.030063	0.029909	0.51	0.395972	0.395875	0.02
0.50	0.009997	0.009952	0.45	0.035455	0.035451	0.01	0.434109	0.434486	0.09
0.55	0.010617	0.010619	0.02	0.039501	0.039614	0.29	0.457064	0.457628	0.12
0.60	0.011091	0.011076	0.14	0.041551	0.041649	0.24	0.466817	0.467288	0.10
0.65	0.011414	0.011721	2.69	0.041279	0.041725	1.08	0.463747	0.463577	0.04
0.70	0.011590	0.011411	1.54	0.038760	0.038369	1.01	0.446573	0.445519	0.24
0.75	0.011624	0.011410	1.84	0.034444	0.034047	1.15	0.411599	0.410388	0.29
0.80	0.011532	0.011234	2.58	0.029053	0.028633	1.45	0.350196	0.348958	0.35
0.85	0.011325	0.010854	4.16	0.023393	0.022785	2.60	0.240750	0.238557	0.91
0.90	0.011022	0.010659	3.29	0.018140	0.017718	2.33	0.085126	0.084241	1.04
0.95	0.010641	0.010686	0.42	0.013707	0.013768	0.45	0.029951	0.030107	0.52
0.99	0.010289	0.010710	4.09	0.010830	0.011260	3.97	0.012487	0.012950	3.71

roughly 29 times faster than the exact method. The relative error in our treatment was only 0.04%. Then we examined the accuracy of the collision efficiency calculated using the *exact* method but with a lower number of expansion terms in order to decrease the computation time. We found that after decreasing the number of terms from 90 to 15, the computation time is still 3 times as long as our integrated model but the relative error is much higher (≈5.5%). With 10 terms, the computation time is only twice as long, compared to our integrated model, but the relative error exceeds 13%. These timing comparisons were done for the case when the number of time steps is relatively small. For a radius ratio close to 0 and when $\lambda \to 1$, our method will be even more efficient.

Next in Fig. 12 we compare our results of collision efficiency with previous results of Hocking and Jonas [20] and Davis and Sartor [19]. Both these classical studies considered droplet rotation. Overall, our results are similar to these earlier results. However, when compared to the exact results shown in Fig. 12, it is clear that our results are much more accurate than the previous results. In our numerical integration of droplet motion, we employed a highly accurate 5th order Runge–Kutta

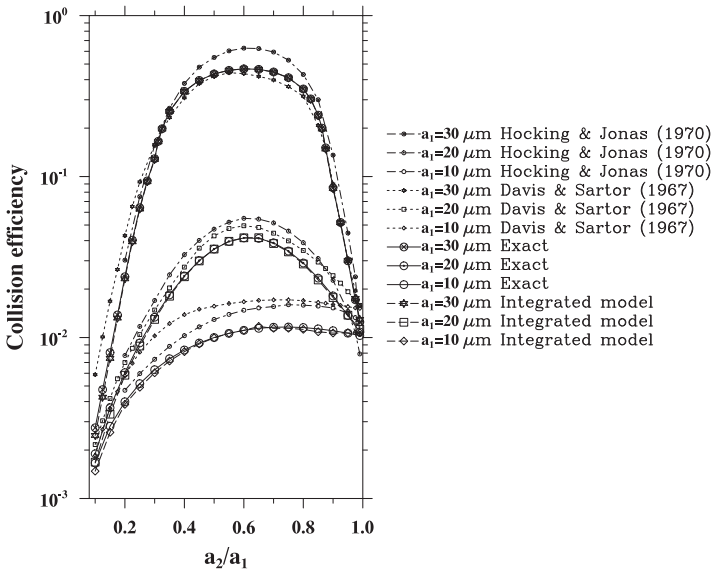

Fig. 12. Collision efficiency as a function of radius ratio for different methods. The exact collision efficiency is calculated based on the full analytical two-body force and torque representation of JO84. Droplet rotation is considered in all cases.

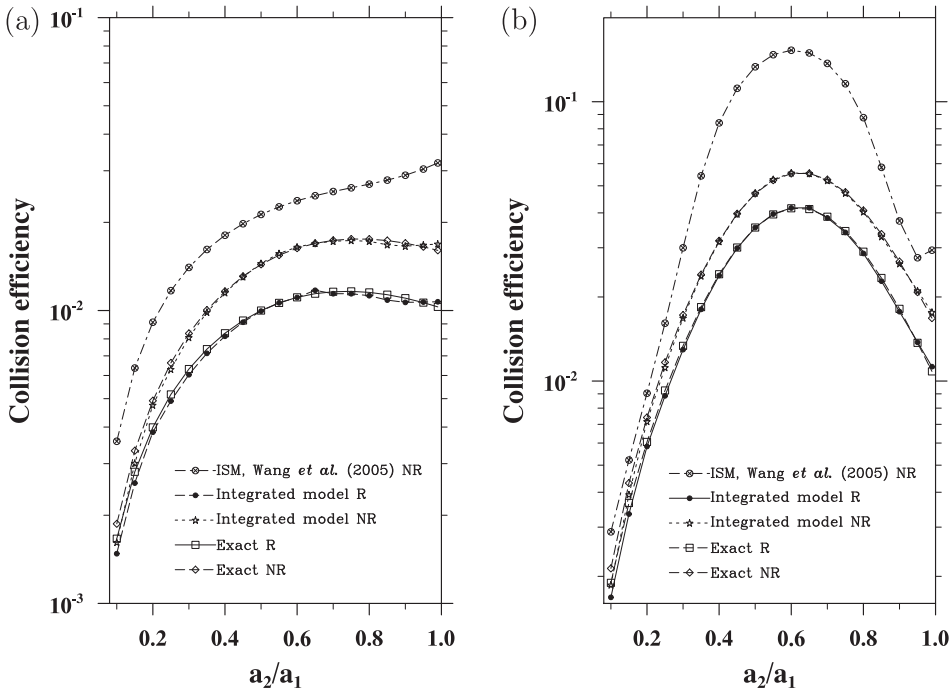

Fig. 13. A comparison of collision efficiency with previously published results. (a) a_1 = 10 μm; (b) a_1 = 20 μm.

scheme with adaptive time step. We also tested 4th order Runge–Kutta and 4th order Adams–Bashforth scheme using small but constant time step sizes. In all cases, we were able to obtain identical results by using small enough time step sizes. In the process, we found that numerical integration errors can lead to an overestimation of the collision efficiency, partly due to the inability for an inaccurate time integration scheme to fully capture the effect of the rapidly varying lubrication force on the motion of droplets at short separations. Both numerical integration errors and non-exact force/torque representation in the earlier studies might have contributed to the small but finite errors in their predictions of the collision efficiency.

In Fig. 13, the results of the improved superposition method (ISM) in [8] are plotted against our results for two different a_1 values. Clearly, ISM significantly overestimates the true collision efficiency due to the inaccurate treatment of the lubrication force and the neglect of droplet rotation. The integrated model developed here adequately addresses both problems in ISM. We found, however, the force representation by ISM is reasonably accurate for long-range interactions (see Figs. 5–10).

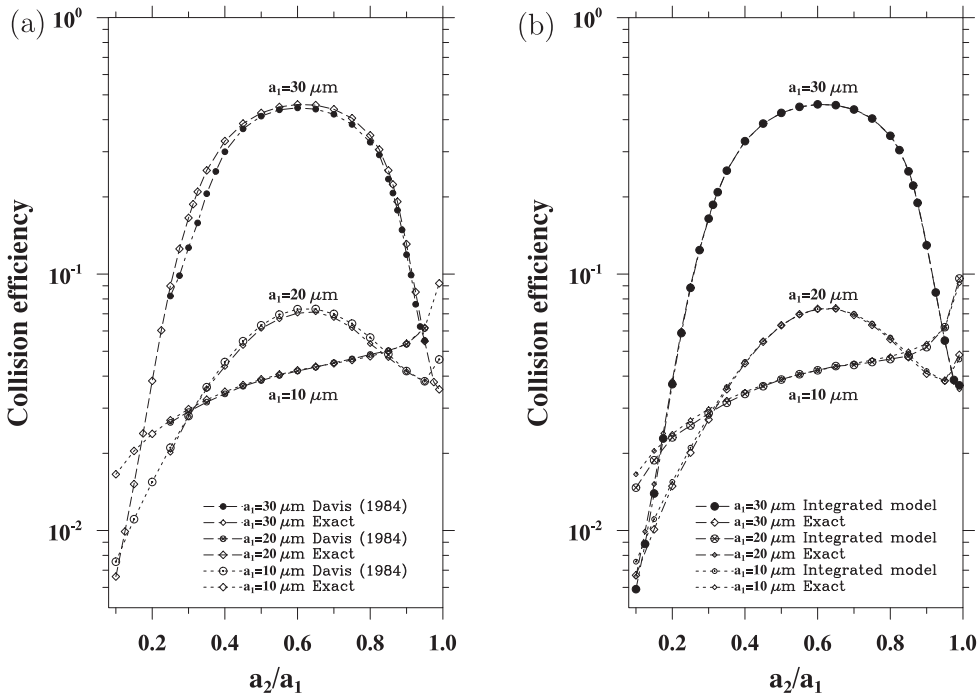

Fig. 14. Collision efficiency from different methods when the van der Waals forces is considered with Hamaker constant set to $5*10^{-20}$ J. (a) Comparison of results based on the exact force and torque representation of JO84 with those obtained in [21]. (b) Comparison of results calculated using our integrated model with the exact results of JO84. Note that Davis [21] assumed an air density of 1.3 kg m^{-3}. Since the results only depend on $\rho_p - \rho$ and $\rho_p \gg \rho$, there is essentially no difference if we use ρ = 1.3 kg m^{-3} or ρ = 1.0 kg m^{-3} here.

Table 9
Calculated collision efficiencies compared to those based on the exact JO84 solution when Van der Waals force is considered. Droplet rotation is not considered.

a_2/a_1	Drop radius a_1 (μm)								
	10 μm			20 μm			30 μm		
	Exact	Our approach	R.E. %	Exact	Our approach	R.E. %	Exact	Our approach	R.E. %
0.10	0.016813	0.014652	12.85	0.007870	0.006877	12.62	0.007057	0.006301	10.71
0.15	0.021059	0.019225	8.71	0.011904	0.010830	9.02	0.016815	0.015512	7.75
0.20	0.024970	0.024208	3.05	0.017129	0.016573	3.25	0.043070	0.041955	2.59
0.25	0.028663	0.027237	4.98	0.023863	0.022863	4.19	0.098267	0.096698	1.60
0.30	0.032149	0.031195	2.97	0.032279	0.031475	2.49	0.172740	0.171643	0.64
0.35	0.035408	0.034872	1.51	0.042265	0.041752	1.21	0.256041	0.255524	0.20
0.40	0.038413	0.038014	1.04	0.053270	0.052901	0.69	0.331290	0.330971	0.10
0.45	0.041141	0.040993	0.36	0.064295	0.064104	0.30	0.387270	0.387184	0.02
0.50	0.043581	0.043932	0.81	0.074101	0.074337	0.32	0.425616	0.426000	0.09
0.55	0.045735	0.046337	1.32	0.081509	0.081999	0.60	0.449085	0.449678	0.13
0.60	0.047621	0.048060	0.92	0.085638	0.086031	0.46	0.459341	0.459844	0.11
0.65	0.049282	0.049290	0.02	0.086034	0.085918	0.13	0.456753	0.456627	0.03
0.70	0.050788	0.050435	0.70	0.082744	0.082105	0.77	0.440200	0.439165	0.24
0.75	0.052253	0.051759	0.95	0.076336	0.075675	0.87	0.406476	0.405284	0.29
0.80	0.053868	0.052929	1.74	0.067864	0.067075	1.16	0.348972	0.347755	0.35
0.85	0.055985	0.054152	3.27	0.058746	0.057437	2.23	0.257106	0.255083	0.79
0.90	0.059434	0.058048	2.33	0.050605	0.049692	1.80	0.145648	0.144370	0.88
0.95	0.067178	0.068173	1.48	0.045647	0.046206	1.22	0.066831	0.067386	0.83
0.99	0.096611	0.101629	5.19	0.052592	0.055235	5.03	0.042629	0.044589	4.60

Now we shall drop the finite-gap model and instead consider explicitly the van der Waals attractive force following the study of Davis [21]. An additional force is added to the equation of motion, Eq. (1), and is given as

$$\mathbf{F}_{vdW} = -\nabla \cdot \Phi_{vdW}, \tag{26}$$

where the force potential is assumed to be [21]

$$\Phi_{vdW} = -\frac{H}{6}\left[\frac{8\lambda}{(s^2-4)(1+\lambda)^2} + \frac{8\lambda}{s^2(1+\lambda)^2 - 4(1-\lambda)^2} + \ln\left\{\frac{(s^2-4)(1+\lambda)^2}{s^2(1+\lambda) - 4(1-\lambda)^2}\right\}\right]. \tag{27}$$

Table 10
Calculated collision efficiencies compared to those based on the exact JO84 solution when van der Waals force is considered. Droplet rotation is considered.

a_2/a_1	Drop radius a_1 (μm)								
	10 μm			20 μm			30 μm		
	Exact	Our approach	R.E. %	Exact	Our approach	R.E. %	Exact	Our approach	R.E. %
0.10	0.016565	0.014692	11.31	0.007557	0.006690	11.47	0.006610	0.005905	10.67
0.15	0.020419	0.018795	7.95	0.011068	0.010094	8.80	0.015166	0.013937	8.10
0.20	0.023807	0.023066	3.11	0.015464	0.014895	3.68	0.038328	0.037201	2.94
0.25	0.026896	0.025659	4.60	0.021031	0.020108	4.39	0.089893	0.088362	1.70
0.30	0.029740	0.028630	3.73	0.027956	0.027083	3.12	0.165625	0.164509	0.67
0.35	0.032357	0.031480	2.71	0.036210	0.035527	1.89	0.253661	0.253131	0.21
0.40	0.034748	0.034078	1.93	0.045404	0.044894	1.12	0.330185	0.329847	0.10
0.45	0.036911	0.036528	1.04	0.054738	0.054454	0.52	0.386426	0.386320	0.03
0.50	0.038850	0.038787	0.16	0.063136	0.063128	0.01	0.424858	0.425211	0.08
0.55	0.040577	0.040685	0.27	0.069505	0.069697	0.28	0.448353	0.448912	0.12
0.60	0.042114	0.042144	0.07	0.072980	0.073141	0.22	0.458597	0.459072	0.10
0.65	0.043506	0.043779	0.63	0.073102	0.073403	0.41	0.455962	0.455810	0.03
0.70	0.044824	0.044208	1.37	0.069936	0.069227	1.01	0.439314	0.438252	0.24
0.75	0.046182	0.045390	1.71	0.064084	0.063318	1.20	0.405413	0.404183	0.30
0.80	0.047767	0.046596	2.45	0.056575	0.055717	1.52	0.347499	0.346234	0.36
0.85	0.049939	0.047931	4.02	0.048694	0.047390	2.68	0.253711	0.251615	0.83
0.90	0.053547	0.051881	3.11	0.041858	0.040854	2.40	0.130888	0.129553	1.02
0.95	0.061636	0.062063	0.69	0.038191	0.038363	0.45	0.054772	0.055022	0.46
0.99	0.092012	0.096122	4.47	0.046457	0.048388	4.16	0.035494	0.036818	3.73

For water droplets in air, the Hamaker constant H is set to 5×10^{-20} J. Fig. 14 shows the collision efficiency after the above van der Waals force is added. Results based on both the exact Stokes force/torque solutions of JO84 and our integrated model are presented and compared to the results of Davis [21]. We find that the three results are all in good agreement, showing that both our integrated model and Davis' calculations are very accurate. Comparison of Figs. 14 and 12 (see also Tables 8 and 10) shows that the direct treatment of the van der Waals force yields different values of collision efficiency, particularly when droplets are small in size ($a_1 \leqslant 20$ μm). When the radius ratio is very small or close to one, the direct incorporation of the van der Waals force leads to larger collision efficiency. For example, for $a_1 = 20$ μm and $\lambda = 0.5$, we obtained a collision efficiency of 0.0631 (Table 10) while the finite-gap model led to a value of 0.0355 (Table 8). When $a_1 = 10$ μm and $\lambda = 0.5$, these are 0.0388 (Table 10) and 0.0100 (Table 8), respectively. The larger efficiency with the van der Waals force indicates that the van der Waals force can play a significant role at a separation larger than $0.001a_1$ assumed in the finite-gap model. These differences are larger than the differences shown in [21] between the calculations with the van der Waals force and those with the Maxwell-slip flow model of Davis [32] and Hocking [33]. In other words, the finite-gap model is less accurate than the Maxwell-slip flow model. The shape of the collision efficiency curve for $a_1 = 10$ μm in Fig. 14 is qualitatively different from that in Fig. 12. For small radius ratio, the van der Waals force leads to a much slower decrease of collision efficiency with decreasing a_2/a_1. When $a_2/a_1 \to 1$, the van der Waals force leads to a second maximum on the curve not present in Fig. 12. In this limit, since the two droplets have a small relative motion, they could spend a long time together at short separations, making the cumulative effect of the van der Waals force relatively more important in leading to collision–coalescence.

The collision efficiency data from different methods are also tabulated in Tables 7–10, both for the purpose of future benchmarking and quantitative inter-comparison. In all these tables, relative errors when compared to the exact treatment are computed. As discussed before, it is believed that the numerical integration errors are negligible in predicted collision efficiency data based on both the exact JO84 force/torque solutions and our integrated model. The relative errors of collision efficiency based on our integrated model are typically less than 5% when radius ratio is larger than 0.2. For very small radius ratio, $a_2/a_1 < 0.2$, the relative error can reach 10% to 15%. In this limit, the aerodynamic interaction force on the smaller droplet in the pair is very strong when compared to the corresponding far-field Stokes drag, e.g., see Figs. 5–8, and at the same time the interaction time is short due to the relatively large relative translational motion. This combination requires accurate force/torque formulation and small numerical integration error if accurate collision efficiency is to be predicted.

For the case with rotation we observed that the relative error is comparable with the case without rotation. This suggests that the main source of errors comes from force calculation in the model.

4. Summary and conclusions

An important issue in cloud microphysics is the accurate calculation of the collision efficiency of cloud droplets. The collision efficiency depends sensitively on the droplet size and could change by several orders of magnitude. In general, the near-field interaction of droplets is a multi-scale problem that couples the droplet inertial effect to local aerodynamic

lubrication force to attractive coalescing force. A simultaneous consideration of droplet inertia and rapidly changing lubrication force is thus required to accurately determine the collision efficiency. Previously no efficient method was made available for accurate determination of the collision efficiency.

Motivated by a need to improve the representation of short-range interaction forces in the HDNS approach of Ayala et al. [9], we have developed an efficient method to evaluate the aerodynamic interaction forces and torques between two droplets settling in a gravitational field. Our method combines the FTS multipole expansion of Durlofsky et al. [12] for the long-range interaction with lubrication expansion at short separations. Explicit FTS formula for computing the forces and torques have been developed for each elemental configuration shown in Fig. 1 and these are compiled in Appendix B. It should be noted that most previous applications of the FTS formulation have been to equal-size particles, while this paper addresses the more general problem of unequal-size particles. A few typos and inconsistencies in JO84 regarding the details of the lubrication expansions have been identified and these are listed in Appendix C. In some cases, the JO84 lubrication expansions have been extended to include higher-order terms for better accuracy and these are given in Tables 3 and 4. A method for treating the intermediate separations using polynomial fitting has been developed and optimized. Since the degree of force/torque singularity as the gap distance approaches zero is different for different elemental configurations shown in Fig. 1, for best accuracy it was necessary to apply different forms of polynomial fitting. After optimizing the matching locations s_1 and s_2, we have demonstrated that the integrated model yields an accurate force and torque representation. The formulation and results developed here are applicable to interactions of all rigid spherical particles in a Stokes flow.

We then applied our model to the determination of collision efficiencies of sedimenting cloud droplets in otherwise stagnant air. The resulting collision efficiencies are in excellent agreement with those based on the exact Stokes flow solution developed by Jeffrey and Onishi [17], with a relative error of typically 2% or less for most cases. The largest relative error does not exceed 18% (note that 18% is not significant since the collision efficiency itself can vary by several orders of magnitude). This is achieved at a small fraction of the computational time needed for the exact treatment. The level of accuracy represents a significant improvement over the improved superposition method [8] that was used in the HDNS approach of Ayala et al. [9].

To our knowledge, the calculated collision efficiencies based on the JO84 exact force representation are new and they have been tabulated for future benchmarking. These data are slightly more accurate than the results in [21]. Guided by the exact results, careful comparisons with the classical results of Davis and Sartor [19] and Hocking and Jonas [20] have been performed, which led to the conclusion that some small but finite corrections to these results are needed. In several cases, we have been able to extend the range of the collision efficiency data to $a_2/a_1 \to 0$, the regime where the collision efficiency is very low and as thus the computation is more expensive. The results of these efforts have been documented as tabulated data in Tables 7–10.

We found the droplet rotation tends to reduce the collision efficiency, particularly for small droplets of similar size. Davis and Sartor [19] commented very briefly on the effect of droplet rotation on collision efficiency by comparing their own results with rotation with the earlier results of Hocking [34] without rotation, but that comparison was incomplete due to the very limited range of a_2/a_1 studied in Hocking [34] and other erroneous treatments in Hocking [34], see page 1371 of Davis and Sartor [19] . Here a more complete comparison of results with and without rotation has been made to illustrate the level of errors that would incur if the rotational degrees of freedom were omitted in the calculation. For larger droplets ($a_1 > 30$ μm), the effect of rotation is only of secondary importance.

In order to simplify the time integration, most previous calculations of collision efficiency used a finite gap to model the effect of very short-range molecular attractive interaction such as the van der Waals force that eventually led to coalescence. Here we repeated the calculation in [21] by explicitly considering the van der Waals force. For droplets of either similar or very difference sizes, we found that a precise treatment of the coalescence force such as van der Waals interaction force is necessary. Namely, the simplified finite-gap model could lead to significant errors in collision efficiency for small cloud droplets. Fortunately, as a result of larger collision efficiency values, the effect of droplet rotation appears to be less important when the van der Waals force is considered (see data in Table 10 vs. Table 9), than in the finite-gap model (see data in Table 8 vs. Table 7).

In future work we hope to apply this efficient and accurate method to study aerodynamic interactions of many droplets in a turbulent background flow, in order to improve the accuracy of the HDNS approach. For cloud physics application, the motion of a very large number of interacting droplets in a turbulent air flow must be simulated to match the realistic cloud water content, therefore, efficient computation of interacting forces is crucial. In general, *accurate* determination of turbulent collision efficiency of cloud droplets remains to be a largely unsolved problem, since the methodology for treating aerodynamic interactions at all separations in a turbulent background flow is yet to be developed. Yeo and Maxey [35] has recently developed an accurate method to include lubrication forces in a many-body system. This and other related methods could be applied to extend our approach to treat the interactions of multiple droplets in a turbulent flow.

Acknowledgments

This study has been supported by the National Science Foundation through Grants ATM-0527140 and ATM-0730766, National Natural Science Foundation of China (NSFC 10628206), and by the National Center for Atmospheric Research (NCAR).

NCAR is sponsored by the National Science Foundation. We are also grateful to Professor David Jeffrey for his valuable explanation of the details of Jeffrey and Onishi [17] and related efficient computational subroutines for reproducing the results in Jeffrey and Onishi [17]. He also helped confirm the typographic errors and inconsistencies in JO84 that are noted in Appendix C.

Appendix A

List of Symbols

a_1, a_2	Droplet radii (μm)
$\bar{a}$	Average value of the droplet radii $\bar{a} = 0.5(a_1 + a_2)$ (μm)
A, B, C, D	Coefficients of the polynomial forms used to fit force and torque over the intermediate separation
CRE	Cumulative relative error
e'_{ij}	Rate of strain of the disturbance flow due to particles – Durlofsky et al. [12]
$\mathbf{E}$	Rate of strain of the background flow – Durlofsky et al. [12]
$\mathbf{F}$	Force exerted by the fluid on the droplets (N)
$\mathbf{F}_{vdW}$	Attracting van der Waals force acting on the droplets (N)
g	Gravitational constant ($g = 9.8$ m s^{-2})
H	Hamaker constant (5×10^{-20} J)
I_p	Moment of inertia (kg μm^2)
J_{ij}	Free-space Green function – [30]
l	Initial vertical separation distance (m)
$\mathbf{L}$	Torque exerted by the fluid on the droplets (J)
m_p	Mass of the droplet (kg)
N_p	Number of interacting droplets
r	Distance between centers of the droplets (m)
$\mathbf{R}$	Rotlet – Durlofsky et al. [12]
s	Normalized distance between centers of the droplets $s = r/\bar{a}$
s_1, s_2	Location of the matching points
$\mathbf{S}$	Stress – Durlofsky et al. [12]
t	Time (s)
$\mathbf{u}$	Velocity disturbance acting on the droplet due to motion of other droplet in its vicinity (m s^{-1})
$\mathbf{V}$	Actual droplet velocity (m s^{-1})
$\mathbf{W}$	Droplet terminal velocity (m s^{-1})
$\mathbf{x}$	Location of arbitrary point in considered domain
$\mathbf{Y}$	Actual droplet location (m,m,m)

Greek letters

α	Droplet index {1,2}
ϵ	Nondimensional separation between surfaces of the two interacting droplets $\epsilon = s - 2$
ϵ_{ijk}	Antisymmetric tensor
ρ	Air density
ρ_p	Droplet density
μ	Air viscosity $\mu = 1.7 * 10^{-5}$ (kg m^{-1} s^{-1})
τ_p	Droplet inertia response time (s)
τ_k	Kolmogorov time of the air turbulence (s)
λ	the ratio of droplet radii, a_2/a_1
δ	initial horizontal displacement (m)
$\mathbf{\Omega}$	Angular droplet velocity (s^{-1})
Φ_{vdW}	Potential of van der Waals force (N s)

Superscipts

∞	Background value or far field when the local disturbance of air flow due to droplets can be neglected

Appendix B

For each of the cases shown in Fig. 1, we apply Eqs. (7) and (8) together and simplify the formulation to an explicit linear system. Without loss of generality, it is assumed that each of the configurations lies in the y–z or x_2–x_3 plane, with x_2 being the horizontal axis pointing to the right, and x_3 the vertical axis pointing downward.

For Case 1 and Case 2, the formulation reduces to a second-order coupled linear system for the drag forces in the vertical direction:

$$\begin{aligned}6\pi\mu a_1 V_3^{(1)}\Delta = {} & F_3^{(1)}\left\{\Delta-\left[\frac{9a_1}{4r}-\frac{9a_1}{20}\left(\frac{5a_1^2+3a_2^2}{r^3}\right)\right]\left(\frac{2a_2^3}{r^3}-\frac{2a_2^3}{5r^3}(3a_2^3+5a_1^2)\right)\frac{6}{5}\right\}\\ & +F_3^{(2)}\left\{\Delta\left[\frac{3a_1}{2r}-\frac{a_1(a_1^2+a_2^2)}{2r^3}\right]+\left[\frac{9a_1}{4r}-\frac{9a_1}{20}\left(\frac{5a_1^2+3a_2^2}{r^3}\right)\right]\right.\\ & \left.\times\left(\frac{6a_2^3}{r^3}-\frac{36}{5}\frac{a_2^3}{r^3}\left(\frac{a_1^2+a_2^2}{r^2}\right)\right)\left(\frac{2a_1^3}{r^3}-\frac{2a_1^3}{5r^3}\frac{3a_1^2+5a_2^2}{r^2}\right)\right\},\end{aligned} \tag{28}$$

$$\begin{aligned}6\pi\mu a_2 V_3^{(2)}\Delta = {} & F_3^{(2)}\left\{\Delta-\left[\frac{9a_2}{4r}-\frac{9a_2}{20}\left(\frac{5a_2^2+3a_1^2}{r^3}\right)\right]\left(\frac{2a_1^3}{r^3}-\frac{2a_1^3}{5r^3}(3a_1^3+5a_2^2)\right)\frac{6}{5}\right\}\\ & +F_3^{(1)}\left\{\Delta\left[\frac{3a_2}{2r}-\frac{a_2(a_2^2+a_1^2)}{2r^3}\right]+\left[\frac{9a_2}{4r}-\frac{9a_2}{20}\left(\frac{5a_2^2+3a_1^2}{r^3}\right)\right]\right.\\ & \left.\times\left(\frac{6a_1^3}{r^3}-\frac{36}{5}\frac{a_1^3}{r^3}\left(\frac{a_1^2+a_2^2}{r^2}\right)\right)\left(\frac{2a_2^3}{r^3}-\frac{2a_2^3}{5r^3}\frac{3a_2^2+5a_1^2}{r^2}\right)\right\},\end{aligned} \tag{29}$$

where

$$\Delta=\frac{36}{25}-\left(6-\frac{36}{5}\frac{a_1^2+a_2^2}{r^2}\right)^2\frac{a_1^3a_2^3}{r^6}, \tag{30}$$

r is the distance between the sphere centers. Only drag forces along the line of centers are non-zero. Forces exerted by the fluid on the particles can be obtained by solving the linear system of second order. Specifically, for Case 1, we set $V_3^{(1)}=V^{(1)}$, $V_3^{(2)}=-V^{(2)}$, $F_3^{(1)}=-F^{(1)}$, and $F_3^{(2)}=F^{(2)}$. While for Case 2, $V_3^{(1)}=V^{(1)}$, $V_3^{(2)}=V^{(2)}$, $F_3^{(1)}=-F^{(1)}$, and $F_3^{(2)}=-F^{(2)}$. Note that in our decomposition, the velocities have the same magnitude, but the expressions above are more general in that they can be applied to velocities of different magnitudes. Torques are not present in Cases 1 and 2.

For Case 3 and Case 4, the following sixth-order linear system is derived:

$$6\pi\mu a_1 V_2^{(1)}=F_2^{(1)}+\left(\frac{3a_1}{4r}+\frac{a_1(a_1^2+a_2^2)}{4r^3}\right)F_2^{(2)}+\frac{3a_1}{4r}\left(\frac{L_1^{(2)}}{r}\right)+\frac{3}{10}\frac{a_1(5a_1^2+3a_2^2)}{r^3}\left(\frac{S_{12}^{(2)}}{r}\right), \tag{31}$$

$$6\pi\mu a_2 V_2^{(2)}=\left(\frac{3a_2}{4r}+\frac{a_2(a_1^2+a_2^2)}{4r^3}\right)F_2^{(1)}+F_2^{(2)}-\frac{3a_2}{4r}\left(\frac{L_1^{(1)}}{r}\right)-\frac{3}{10}\frac{a_2(5a_2^2+3a_1^2)}{r^3}\left(\frac{S_{12}^{(1)}}{r}\right), \tag{32}$$

$$0=\frac{a_1^3}{r^3}F_2^{(2)}-\left(\frac{L_1^{(1)}}{r}\right)+\frac{1}{2}\frac{a_1^3}{r^3}\left(\frac{L_1^{(2)}}{r}\right)+3\frac{a_1^3}{r^3}\left(\frac{S_{12}^{(2)}}{r}\right), \tag{33}$$

$$0=\frac{a_2^3}{r^3}F_2^{(1)}-\frac{1}{2}\frac{a_2^3}{r^3}\left(\frac{L_1^{(1)}}{r}\right)+\left(\frac{L_1^{(2)}}{r}\right)-3\frac{a_2^3}{r^3}\left(\frac{S_{12}^{(1)}}{r}\right), \tag{34}$$

$$0=\frac{a_1^3}{6}\frac{(3a_1^2+5a_2^2)}{r^5}F_2^{(2)}+\frac{5a_1^3}{4r^3}\left(\frac{L_1^{(2)}}{r}\right)-\left(\frac{S_{12}^{(1)}}{r}\right)-\left[\frac{5}{2}\frac{a_1^3}{r^3}-\frac{4(a_1^2+a_2^2)a_1^3}{r^5}\right]\left(\frac{S_{12}^{(2)}}{r}\right), \tag{35}$$

$$0=\frac{a_2^3}{6}\frac{(3a_2^2+5a_1^2)}{r^5}F_2^{(1)}-\frac{5a_2^3}{4r^3}\left(\frac{L_1^{(1)}}{r}\right)+\left[\frac{5}{2}\frac{a_2^3}{r^3}-\frac{4(a_1^2+a_2^2)a_2^3}{r^5}\right]\left(\frac{S_{12}^{(1)}}{r}\right)+\left(\frac{S_{12}^{(2)}}{r}\right). \tag{36}$$

Forces and torques acting on the particles can be found by solving the system after replacing variables $V_2^{(1)}=-V^{(1)}$, $V_2^{(2)}=V^{(2)}$, $F_2^{(1)}=F^{(1)}$, $F_2^{(2)}=-F^{(2)}$, $L_1^{(1)}=-L^{(1)}$, $L_1^{(2)}=-L^{(2)}$ in Case 3, and $V_2^{(1)}=-V^{(1)}$, $V_2^{(2)}=-V^{(2)}$, $F_2^{(1)}=-F^{(1)}$, $F_2^{(2)}=-F^{(2)}$, $L_1^{(1)}=L^{(1)}$, $L_1^{(2)}=-L^{(2)}$ in Case 4. $V_k^{(\alpha)}$ is the magnitude of k – component velocity for particle α.

For Cases 5 and 6, the following sixth-order linear system is derived:

$$0=F_2^{(1)}+\left(\frac{3a_1}{4r}+\frac{a_1(a_1^2+a_2^2)}{4r^3}\right)F_2^{(2)}-\frac{3a_1}{4r}\left(\frac{L_1^{(2)}}{r}\right)-\frac{3}{10}\frac{a_1(5a_1^2+3a_2^2)}{r^3}\left(\frac{S_{12}^{(2)}}{r}\right), \tag{37}$$

$$0=\left(\frac{3a_2}{4r}+\frac{a_2(a_1^2+a_2^2)}{4r^3}\right)F_2^{(1)}+F_2^{(2)}+\frac{3a_2}{4r}\left(\frac{L_1^{(1)}}{r}\right)+\frac{3}{10}\frac{a_2(5a_2^2+3a_1^2)}{r^3}\left(\frac{S_{12}^{(1)}}{r}\right), \tag{38}$$

$$8\pi\mu a_1^2\Omega_1^{(1)} = \frac{a_1^2}{r^2}F_2^{(2)} + \frac{r}{a_1}\left(\frac{L_1^{(1)}}{r}\right) - \frac{1}{2}\frac{a_1^2}{r^2}\left(\frac{L_1^{(2)}}{r}\right) - 3\frac{a_1^2}{r^2}\left(\frac{S_{12}^{(2)}}{r}\right), \tag{39}$$

$$8\pi\mu a_2^2\Omega_1^{(2)} = -\frac{a_2^2}{r^2}F_2^{(1)} - \frac{1}{2}\frac{a_2^2}{r^2}\left(\frac{L_1^{(1)}}{r}\right) + \frac{r}{a_2}\left(\frac{L_1^{(2)}}{r}\right) - 3\frac{a_2^2}{r^2}\left(\frac{S_{12}^{(1)}}{r}\right), \tag{40}$$

$$0 = \frac{a_1^3}{6}\frac{(3a_1^2+5a_2^2)}{r^5}F_2^{(2)} - \frac{5a_1^3}{4r^3}\left(\frac{L_1^{(2)}}{r}\right) + \left(\frac{S_{12}^{(1)}}{r}\right) + \left[\frac{5}{2}\frac{a_1^3}{r^3} - \frac{4(a_1^2+a_2^2)a_1^3}{r^5}\right]\left(\frac{S_{12}^{(2)}}{r}\right), \tag{41}$$

$$0 = -\frac{a_2^3}{6}\frac{(3a_2^2+5a_1^2)}{r^5}F_2^{(1)} - \frac{5a_2^3}{4r^3}\left(\frac{L_1^{(1)}}{r}\right) + \left[\frac{5}{2}\frac{a_2^3}{r^3} - \frac{4(a_1^2+a_2^2)a_2^3}{r^5}\right]\left(\frac{S_{12}^{(1)}}{r}\right) + \left(\frac{S_{12}^{(2)}}{r}\right). \tag{42}$$

Here forces and torques are induced by the particles rotation $\Omega^{(\alpha)}$. For Case 5, we have $\Omega_1^{(1)} = \Omega^{(1)}$, $\Omega_1^{(2)} = \Omega^{(2)}$, $F_2^{(1)} = F^{(1)}$, $F_2^{(2)} = -F^{(2)}$, $L_1^{(1)} = -L^{(1)}$, $L_1^{(2)} = -L^{(2)}$. And for Case 6 , $\Omega_1^{(1)} = \Omega^{(1)}$, $\Omega_1^{(2)} = -\Omega^{(2)}$, $F_2^{(1)} = -F^{(1)}$, $F_2^{(2)} = -F^{(2)}$, $L_1^{(1)} = L^{(1)}$, $L_1^{(2)} = -L^{(2)}$. Again, different rotational speeds are allowed in the above results.

Appendix C

In this Appendix, we wish to point out that there are several typographic errors and inconsistencies in JO84, as identifying these could take a significant amount of work. It should be noted that some of these errors and inconsistencies have been noted in previous studies. For example, Dance and Maxey [36] compiled the corrected lubrication expansions for two equal-size droplets, see Table 2 in Dance and Maxey [36]. Their results represent a special case shown in Tables 1–5 for two unequal droplets. Dr. David Jeffrey had attempted to post a corrected version of JO84 online, see http://www.apmaths.uwo.ca/~djeffrey/Stokes.html; but the corrected version is no longer available. To our knowledge, the typographic errors and inconsistencies in JO84 have never been formally publicized.

First, a typographic error in one of the recurrence relations, Eq. (4.9) in JO84, was found when we were trying to calculate the coefficients A_{ij}^Y. The correct form for Eq. (4.9) in JO84 should be

$$V_{npq} = P_{npq} + \frac{2n}{(n+1)(2n+3)}\sum_{s=1}^{q}\binom{n+s}{n+1}P_{s(q-s)(p-n-1)}. \tag{43}$$

The last part of indices for the coefficient P should be $(p-n-1)$ instead of $(p-n+1)$ printed in JO84. Eq. (43) is part of recurrence relations needed to calculate coefficients A_{ij}^Y. Moreover this correct form of the recurrence relations is crucial if one wishes to calculate the resistance functions, to any desired accuracy, for arbitrary separation and size ratio of the particle pair. The above equation is also required for calculating B_{ij}^Y and C_{ij}^Y coefficients needed for asymptotic expressions for force and torque in Cases 3 to 6.

Second, all the coefficients B_{ij}^Y listed in Table 5 of JO84 do not match to their definition given by Eq. (5.7) and Eq. (5.8) in JO84.

Third, the values of C_{12}^Y listed in Table 6 of JO84 are different from what would be obtained from Eq. (7.12) for C_{12}^Y, although the values of C_{11}^Y, C_{22}^Y listed in Table 6 of JO84 appear to be correct.

Fourth, there are two more discrepancies in JO84 related to the resistance functions Y_{12}^C and X_{12}^C. The general formulation for Y_{12}^C in Eq. (7.15) of JO84 for any separation does not converge to its asymptotic form given by Eq. (7.10) in JO84, when $s \to 2$.

Finally, there is a typographic error in the definition of resistance function X_{12}^C, Eq. (6.13) of JO84. The correct form of that equation should be

$$X_{12}^C = \frac{4s^{-2}\lambda^2}{(1+\lambda)^4}\ln\frac{(s+2)}{(s-2)} + \frac{8\lambda^2}{(1+\lambda)^4}s^{-1}\ln(1-4s^{-2}) - \frac{8}{(1+\lambda)^3} \times \sum_{k=1}^{\infty}\left\{(1+\lambda)^{-2k-1}f_{2k+1} - (3k-2)2^{2k-1}k^{-1}(2k-1)^{-1}\frac{\lambda^2}{1+\lambda}\right\}s^{-2k-1}. \tag{44}$$

However, X_{12}^C is not needed in the present study, because the gravitational interaction problem does not involve the mutual particle rotation around lines of centers. X_{12}^C would be needed if the more general problem of particle aerodynamic interaction in a turbulent background flow were considered.

References

[1] R.A. Shaw, Particle-turbulence interactions in atmospheric clouds, Ann. Rev. Fluid Mech. 35 (2003) 183–227.
[2] L.P. Wang, W.W. Grabowski, The role of air turbulence in warm rain initiation, Atmos. Sci. Lett. 10 (2009) 1–8.
[3] K.V. Beard, H.T. Ochs, Warm-rain initiation: an overview of microphysical mechanisms, J. Appl. Meteor. 32 (1993) 608–625.

[4] Y. Xue, L.P. Wang, W.W. Grabowski, Growth of cloud droplets by turbulent collision–coalescence, J. Atmos. Sci. 65 (2007) 331–356.
[5] W.W. Grabowski, L.-P. Wang, Diffusional and accretional growth of water drops in a rising adiabatic parcel: effects of the turbulent collision kernel, Atmos. Chem. Phys. 9 (2009) 2335–2353.
[6] L.P. Wang, O. Ayala, B. Rosa, W.W. Grabowski, Turbulent collision efficiency of heavy particles relevant to cloud droplets, New J. Phys. 10 (2008) 075013.
[7] L.P. Wang, O. Ayala, S.E. Kasprzak, W.W. Grabowski, Theoretical formulation of collision rate and collision efficiency of hydrodynamically-interacting cloud droplets in turbulent atmospheres, J. Atmos. Sci. 62 (2005) 2433–2450.
[8] L.P. Wang, O. Ayala, W.W. Grabowski, Improved formulations of the superposition method, J. Atmos. Sci. 62 (2005) 1255–1266.
[9] O. Ayala, W.W. Grabowski, L.-P. Wang, A hybrid approach for simulating turbulent collisions of hydrodynamically-interacting particles, J. Comput. Phys. 225 (2007) 51–73.
[10] L.P. Wang, B. Rosa, H. Gao, G.W. He, G.D. Jin, Turbulent collision of inertial particles: point-particle based, hybrid simulations and beyond, Int. J. Multiphase Flow 35 (2009) 854–867.
[11] L.P. Wang, O. Ayala, W.W. Grabowski, Effects of aerodynamic interactions on the motion of heavy particles in a bidisperse suspension, J. Turbulence 8 (2007) 1–28.
[12] L. Durlofsky, J.F. Brady, G. Bossis, Dynamic simulation of hydrodynamically interacting particles, J. Fluid Mech. 180 (1987) 21–49.
[13] J.F. Brady, G. Bossis, Stokesian dynamics, Ann. Rev. Fluid Mech. 20 (1988) 111–157.
[14] H. Faxen, The resistance against the movement of a rigour sphere in viscous fluids, which is embedded between two parallel layered barriers, Annalen der Physik 68 (1922) 89–119.
[15] M.R. Maxey, J.J. Riley, Equation of motion for a small rigid sphere in a nonuniform flow, Phys. Fluids 26 (1983) 883–889.
[16] K. Ichiki, Improvement of the Stokesian dynamics method for systems with a finite number of particles, J. Fluid. Mech. 452 (2002) 231–262.
[17] D.J. Jeffrey, Y. Onishi, Calculation of the resistance and mobility functions for two unequal rigid spheres in low-Reynolds-number flow, J. Fluid. Mech. 139 (1984) 261–290.
[18] S. Kim, R.T. Mifflin, The resistance and mobility functions of two equal spheres in low-Reynolds-number flow, Phys. Fluids 28 (1985) 2033–2045.
[19] M.H. Davis, J.D. Sartor, Theoretical collision efficiencies for small cloud droplets in Stokes flow, Nature 215 (1967) 1371–1372.
[20] L.M. Hocking, P.R. Jonas, The collision efficiency of small drops, Quart. J. Roy. Meteor. Soc. 96 (1970) 722–729.
[21] R.H. Davis, The rate of coagulation of a dilute polydisperse system of sedimenting spheres, J. Fluid. Mech. 145 (1984) 179–199.
[22] J.D. Klett, M.H. Davis, Theoretical collision efficiencies of cloud droplets at small Reynolds numbers, J. Atmos. Sci. 30 (1973) 107–117.
[23] U. Shafrir, M. Nuiburger, Collision efficiencies of two spheres falling in viscous medium, J. Geophys. Res. 68 (1963) 4141–4147.
[24] U. Shafrir, T.A. Gal-Chen, Numerical study of collision efficiencies and coalescence parameters for droplet pairs with radii up to 300 microns, J. Atmos. Sci. 28 (1971) 741–751.
[25] C. Lin, S. Lee, Collision efficiency of water drops in the atmosphere, J. Atmos. Sci. 32 (1975) 1412–1418.
[26] R.J. Schlamp, S.N. Grover, H.R. Pruppacher, A.E. Hamielec, Numerical investigation of effect of electric charges and vertical external electric-fields on collision efficiency of cloud drops, J. Atmos. Sci. 33 (1976) 1747–1755.
[27] M. Pinsky, A. Khain, M. Shapiro, Collision efficiency of drops in a wide range of Reynolds numbers: effects of pressure on spectrum evolution, J. Atmos. Sci. 58 (2001) 742–764.
[28] H.R. Pruppacher, J.D. Klett, Microphysics of Clouds and Precipitation, second ed., Kluwer Academic, Dordrecht, 1997.
[29] O. Ayala, B. Rosa, L.-P. Wang, W.W. Grabowski, Effects of turbulence on the geometric collision rate of sedimenting droplets: Part 1. Results from direct numerical simulation, New J. Phys. 10 (2008) 075015.
[30] S. Kim, S.J. Karilla, Microhydrodynamics: Principles and Selected Applications, Butterworth-Heinmann, Boston/London, 1991.
[31] A.M. Ardekani, R.H. Rangel, Unsteady motion of two solid spheres in Stokes flow, Phys. Fluids 18 (2006) 103306.
[32] M.H. Davis, Collision of small cloud droplets: gas kinetic effects, J. Atmos. Sci. 29 (1972) 911–915.
[33] L.M. Hocking, The effect of slip on the motion of a sphere close to a wall and of two adjacent spheres, J. Eng. Math. 7 (1973) 207–221.
[34] L.M. Hocking, The collision efficiency of small drops, Quart. J. R. Met. Soc. 85 (1959) 449–485.
[35] K. Yeo, M.R. Maxey, Simulation of concentrated suspensions using the force-coupling method, J. Comput. Phys. 229 (2010) 2401–2421.
[36] S.L. Dance, M.R. Maxey, Incorporation of lubrication effects into the force-coupling method for particulate two-phase flow, J. Comput. Phys. 189 (2003) 212–238.